SLAC-410
SLAC/SSRL 0003
UC-408
(SSRL-M)

X-RAY ABSORPTION SPECTROSCOPIC STUDIES OF THE DINUCLEAR IRON CENTER IN METHANE MONOOXYGENASE AND THE SULFURE AND CHLORINE CENTERS IN PHOTOGRAPHIC MATERIALS*

Jane G. DeWitt

Stanford Linear Accelerator Center
Stanford Synchrotron Radiation Laboratory
Stanford University, Stanford, California 94309

December 1992

Prepared for the Department of Energy under contract number DE-AC03-76SF00515 and the NIH, Biomedial Resource Technology Program, Division of Research Resources

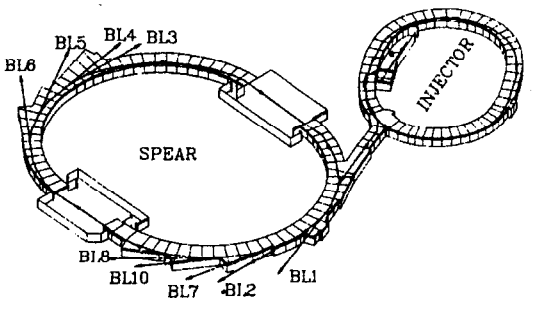

Printed in the United States of America. Available from the National Technical Information Service, U.S. Department of Commerce, 5285 Port Royal Road, Springfield, Virginia 22161

* Ph.D. thesis

Abstract

The Diiron Center in Methane Monooxygenase. The dinuclear iron center of the hydroxylase component of soluble methane monooxygenase (MMO) from *Methylococcus capsulatus* (Bath) and *Methylosinus trichosporium* (OB3b) has been studied by X-ray absorption spectroscopy. Analysis of the Fe K-edge EXAFS revealed that the first shell coordination of the Fe(III)Fe(III) oxidized state of the hydroxylase from *M. capsulatus* (Bath) consists of approximately 6 N and O atoms at an average distance of 2.04 Å. The Fe-Fe distance was determined to be 3.4 Å. No evidence for the presence of a short oxo bridge in the iron center of the oxidized hydroxylase was found, suggesting that the active site of MMO is significantly different from the active sites of the dinuclear iron proteins hemerythrin and ribonucleotide reductase. In addition, the results of the first shell fits suggest that there are more oxygen than nitrogen donor ligands.

The active sites of the photoreduced Fe(III)Fe(II) semimet form of the hydroxylase from both *M. capsulatus* (Bath) and *M. trichosporium* (OB3b) consist of approximately 6 N and O atoms at an average distance of 2.06 - 2.09 Å with an Fe interaction at 3.41 - 3.43 Å. This implies that the diiron center of the hydroxylase from the two species are structurally similar. In addition, the results of the second shell fits to the hydroxylase suggest that there is a shell of low-Z atoms at ~ 3.0 Å in both the diferric and semimet active sites. Upon reduction to the Fe(II)Fe(II) reduced form, the average first shell distance increased to 2.15 Å and the Fe-Fe interaction was no longer detected.

The Fe K-edge EXAFS showed only minor metrical changes in the coordination environment of the hydroxylase iron center due to the presence of substrate and component B, the regulatory protein of the MMO enzyme system. This finding was true for the complexes of semimet and reduced hydroxylase. The changes seen occured in the first coordination sphere. In particular, the presence of component B seemed to have an effect on the distance distribution of first shell atoms. No evidence of a Br contribution was seen in the EXAFS of the hydroxylase in the presence of a brominated substrate. This suggests that the site of interaction between the hydroxylase and substrate is more than 4 Å from the iron center. The presence of substrate and component B was found to modify the Fe K-edge spectra of the hydroxylase. The change seen in the spectra of the semimet samples is consistent with an increase in the covalency of the iron center. The appearance of the edges of the reduced forms of the hydroxylase suggest that the presence of substrate or component B inhibits the reduction of the diferric hydroxylase to a diferrous state. These studies suggest that the changes seen in the hydroxylase diiron site in the presence of

substrate or component B result from subtle perturbations in the coordination environment of the iron atoms accompanied by changes in the electronic structure of the iron center.

Diiron Model Complexes. The analysis of the second shell data of the hydroxylase suggested that the Fe-Fe distance determined may depend on the model compound used in the fits. A detailed investigation of the apparent model bias was therefore performed using nine structurally characterized di- and tri-bridged iron dimers representing a variety of bridging modes and Fe-Fe distances. In general, two minima were found in fits to the second shell data: one at the correct Fe-Fe distance and one ~ 0.4 Å away. The best fit to the second shell data, however, corresponded in every case to the Fe-Fe distance most similar to that of the model compound used to extract the Fe amplitude and phase parameters employed in the fit. This bias reflected only the Fe-Fe distance of the model compound from which the parameters were obtained, and was independent of the number or nature of bridges in the diiron center except as those factors determine the Fe-Fe distance. A strong correlation between the second shell Fe and C parameters was also observed, impacting both the coordination numbers and the distances of the Fe and C contributions. These results illustrate that caution must be used in the interpretation of the results of fits to second shell data from dinuclear iron centers. Similar caution should be used in the analysis of other dinuclear metalloprotein systems as well. Finally, other information must be used in conjunction with EXAFS analysis before any final conclusions can be reached regarding the second shell coordination.

The appearance of Fe K-edge XANES spectra for di- and tri-bridged iron dimers was related to the ligation of the iron center and to the nature of the bridging groups. The position of the edge moved to lower energy with increasing average first shell distance. The spectra of some oxo-bridged models had a shoulder on the rising edge that was not present in the spectra of the non-oxo-bridged models. The appearance of this shoulder in the oxo-bridged dimer spectra was correlated to an increase in the N ligation relative to the O ligation. A reasonable interpretation of this feature is that it is a shake down feature associated with the $1s \rightarrow 4p$ transition, and reflects an increase in the covalency of the iron site due to the change in the ligation. The appearance of the pre-edge feature ($1s \rightarrow 3d$ transition) was characteristic of the nature of the bridge in the diferric models, but not of the number of bridges in the diiron site. In oxo-bridged compounds, the pre-edge feature was asymmetric, while in the non-oxo-bridged compounds, the pre-edge feature was clearly resolved into a doublet. The splitting or asymmetry of this feature is consistent with an assignment of the transition to the $^5T_{2g}$ and ^5E_g molecular states for the excited state d^6 configuration. Greater overall intensity of the pre-edge feature was found for the oxo-bridged models, reflecting the increased distortion of the iron site due to the presence of the

short Fe-O_{oxo} bridge. The appearance of the edge and pre-edge regions of the edge spectra for the oxidized hydroxylase of MMO is consistent with the absence of a μ-oxo bridge in the diiron site and with 6-coordinate iron atoms.

Photographic Materials. The sulfur and chlorine centers in spectral sensitizing dyes and chemical sensitizing centers of importance to the photographic system were characterized by S and Cl K-edge X-ray absorption spectroscopy. This technique was found to be sensitive to the different environments of S in the compounds investigated, as well as to the nature and extent of the interaction between S and Au or Ag metals atoms. In particular, a sharp, intense pre-edge feature seen in the spectra of compounds containing exocyclic S (thione or thiol), is not seen in the spectra of thiazole-containing (cyclic S) compounds. The use of oriented single-crystal studies permitted the assignment of the exocyclic S pre-edge feature as a transition to a S $p\pi^*$ orbital. The main feature in all S K-edge spectra was assigned as a transition to a S $p\sigma^*$ orbital. Cl is present as a substituent on the ring system of the dye molecules. The Cl K-edge spectra changed little, reflecting the similar environments the Cl atom occupies in the compounds studied. Dramatic changes occured in the S K-edge spectra of covalent Ag and Au metal complexes, while ionic interactions with metal atoms resulted in little change in the S spectra. Polarized surface measurements at a glancing angle configuration were done on S species adsorbed on AgBr sheet crystals. These studies clearly show that a bond is not formed between the metal and S atoms. The interaction between the dye molecules and the AgBr substrate is therefore of a physical rather than a chemical nature. In addition, the sensitivity of XAS to the polarization properties of the S and Cl K-edge features provided insight into the orientation of the dye molecules on the AgBr substrate.

Acknowledgements

My graduate school experience was marked by good fortune. I joined the Hodgson group because I thought it would be an interesting and unique opportunity to do synchrotron radiation research, and I was absolutely right. There was nothing quite like the sense of accomplishment I felt when I really knew how to run an XAS experiment. The MMO project opened the door to the fields of environemental science and bioremediation, areas of research in which I plan to continue working. Because of our close affiliation with SSRL, our group had the valuable opportunity to learn more about and be more deeply involved with many different aspects of synchrotron radiation research, as well as to interact with other groups doing research at the facility. Some of us were lucky enough to go through the 1989 NSLS experience. The bright side of NSLS was that after mystery meat pizza on X19A, beamtime could only improve in the future.

I am grateful to a host of people who gave me the support, encouragement and friendship I needed to stay and succeed. First and foremost, I would like to thank my adviser, Keith Hodgson, for the trust he exhibited in my ability to achieve this goal and succeed in this work. His confidence in me bolstered my confidence in myself, an invaluable gift. Keith expects his students to work hard and to be independent, and gives us the freedom to develop as individuals, both scientifically and personally. He provided a working environment in which I could work at my own pace, with enough pressure to insure progress but enough guidance to avoid feeling overwhelmed. The work I did was challenging and rewarding, and I am grateful that I had the good fortune to work with Keith. I am also grateful for the many opportunities Keith gave me to present my work at conferences and to interact with other researchers in the field. I wish him continued years of success, and most importantly, of health.

We are very fortunate in the Hodgson group to be able to work closely with two remarkable people, Britt Hedman and Pat Frank. Britt is a wonderful mentor. She always seems to have the answer, but when asked a question has the unique ability to teach you the answer instead of just telling it to you. Pat always has another way to think about a problem or a result. He reminded me that the more I think I know about something, the more important it is that I question my knowledge and my method of thinking, so that I do not overlook something important. Keith, Britt and Pat represent integrity and dedication in science, and I am so grateful to have learned about the scientific process from them.

I also want to acknowledge and thank the people in the Hodgson group: David Eliezer, Grace Tan, Chrisie Stanfel, Lingling Chen, Kent Nakagawa, Tami Westre, Isaac Liu and Susan Shadle. They are terrific people and I am glad that I was fortunate enough

to work with them and get to know them. I wish them all successful and speedy experiments in the future. I also want to acknowledge the contributions of the collaborators on the MMO project: Prof. Stephen J. Lippard, Dr. James G. Bentsen, and Amy C. Rosenzweig. I thank them for the reliable delivery of MMO samples. I hope the crystal structure is coming along well. In addition, I want to thank the staff at SSRL, especially Robert Mayer. They are a talented, dedicated group of people and make beamtime a much more successful and enjoyable experience.

Terre Smith was the collaborator on the photo project and continues to be a good friend. She and I always managed to find the worst restaurant, and always managed to pick the worst thing on the menu. I look forward to finding bad restaurants in New Mexico with her. Claire Conway never stopped trying to get me to come up to the city. I've enjoyed getting to know her better and am thankful for her sympathetic ear. I hope that we can find each other again when she gets back from her trip around the world. Brooke Hemming, Tami Westre and Susan Shadle have saved my sanity and given me more support and shored up my self-esteem more than they know. I thank them for the fun, interesting and spirited conversations and for the sense of community and growth that their friendship provides me. I am especially grateful for Susan's friendship and honest perspective on the world. Carl Brown contributed ABBA, Led Zeppelin, disco and lima beans to my stay at Stanford. I have appreciated his friendship and sense of humor. I thank Erin Grant, who has always been and continues to be a source of honesty and friendship, for rescuing me more than once during these past few years. Larry Meixner is very special to me, and I thank him for his unfailing belief in me, for his support and encouragement and his friendship all of these years.

Finally, I want to thank my family for all that they have given me. It has been very important to me to have been within two hours of my family during these years. I thank my sister and brother-in-law, Karen DeWitt-Mattei and Scott Mattei; my step-sister and uncle, Tracy and Tom Barber; and my nephews and niece, Nick Mueller and Donny and Jessica Barber; for all of the support and fun and distractions and for being there for me. For their unconditional support and faith, I thank my mom and step-dad, Marsha and Fred Mueller. I thank my dad, Grigg DeWitt, for his constant curiosity and encouragement. I did this for myself, but I could not have done this without them. They gave me the courage to start on this path, and so this work is dedicated to my family.

Contents

Abstract ii
Acknowledgements v
Contents vii
List of Tables xi
List of Figures xiii
List of Abbreviations xvii

Chapter 1 Introduction to the Methane Monooxygenase Enzyme System and the EXAFS Analysis Method 1

1.1. Scope and Organization of this Dissertation 2
1.2. Methanotrophic Bacteria 3
1.3. The Soluble Methane Monooxygenase Enzyme System 5
1.4. Spectroscopic Studies of Dinuclear Non-Heme Iron Centers 7
1.5. X-ray Absorption Spectroscopy 9
1.5.1. Extended X-ray Absorption Fine Structure 11
1.5.2. Data Reduction and Analysis 15
1.6. References and Notes 21

Chapter 2 X-ray Absorption Spectroscopic Studies of the Dinuclear Non-Heme Iron Center in the Hydroxylase Component of Methane Monooxygenase and the B2 Subunit of Ribonucleotide Reductase 25

2.1. Introduction 26
2.2. Experimental 28
2.2.1. EXAFS Sample Preparation 28
2.2.2. Data Collection, Reduction and Analysis 28
2.3. Results of XAS Experiments 31
2.3.1. Photoreduction of the Oxidized Hydroxylase 35
2.3.2. Results of Fits to the Hydroxylase EXAFS Data 35
2.3.2.1. First Shell Fits 35
2.3.2.2. Second Shell Fits 39
2.3.2.3. Wide Shell Fits 45

2.3.2.4. Model Dependence of EXAFS Results 45
2.3.2.5. Fits to the Unfiltered Data 50
2.3.2.6. Fits Over a Shorter Data Range 50
2.3.3. Results of Fits to the Ribonucleotide Reductase EXAFS Data 52
2.4. Discussion 52
2.4.1. Nature of the Hydroxylase Active Site 52
2.4.2. Comparisons to Proteins Containing Diiron Cores 56
2.5. Conclusions 58
2.6. Acknowledgements 59
2.7. References and Notes 60

Chapter 3 Structural Studies of the Diiron Center in Methane Monooxygenase in the Presence of Substrate and the Regulatory Protein of the MMO Enzyme System 64

3.1. Introduction 65
3.2. Experimental 67
3.2.1. EXAFS Sample Preparations 67
3.2.2. EXAFS Data Collection, Reduction and Analysis 68
3.3. Results of XAS Experiments 70
3.3.1. Photoreduction of the Oxidized Hydroxylase Samples 76
3.3.2. Results of Fits 76
3.3.2.1. First Shell Fits 76
3.3.2.2. Second Shell Fits 83
3.3.2.3. Wide Shell Fits 89
3.3.2.4. The Origin of the Metrical Differences in the EXAFS 93
3.3.2.5. Fits to the Non-Filtered Data 93
3.3.3. X-ray Absorption Near Edge Spectra 102
3.4. Discussion 107
3.4.1. The Empirical Fitting Proceedure 107
3.4.2. The Effect of Substrate and Component B on the Structure of the Diiron Center 109
3.4.2.1. Changes in the Coordination Sphere of the Iron Center 110

3.4.2.2. Interpretation of the Hydroxylase Edge Spectra 115
3.5. Conclusions 117
3.6. Acknowledgements 117
3.7. References and Notes 118

Chapter 4 An Investigation of the Model Dependency of EXAFS Data Analysis for Dinuclear Non-Heme Iron Systems 122

4.1. Introduction 123
4.2. Experimental 124
4.3. Results of Fits to the Model Data 130
4.3.1. A Description of the Trends Seen in First Shell Fits 131
4.3.2. The Dependence of Second Shell Fits on Choice of Model Compound 144
4.3.2.1. Investigation with Model Data. 144
4.3.2.2. Correlations with Second Shell Low-Z Atoms 152
4.3.2.3 Investigations with Hydroxylase Data 157
4.4. Discussion 158
4.4.1. Interpretation of First Shell Fits 158
4.4.2. Model-Dependent Results of Second Shell Fits 162
4.4.2.1. Model Compounds 162
4.4.2.2. The Hydroxylase Active Site 167
4.4.2.3. Survey of Other Second Shell Analysis Methods 168
4.5. Conclusions 169
4.6. Acknowledgements 170
4.7. References and Notes 172

Chapter 5 Fe K-Edge X-ray Absorption Edge Spectra of Iron Models Relevant to Dinuclear Non-Heme Iron Enzyme Systems 175

5.1. Introduction 176
5.1.1. Interpretation of Transition Metal XANES Spectra 176
5.2. Experimental 177

5.3. Results and Discussion 179
5.3.1. Description of the Edge Spectra. 180
5.3.1.1. Models Containing a μ-oxo Bridge 180
5.3.1.2. Non-oxo Bridged Models 185
5.3.1.3. Changes in Spectra with Oxidation State 187
5.3.2. Interpretation of Edge Spectra 190
5.3.2.1. Changes in the Edge Spectra with Bridging Geometry 190
5.3.2.2. Changes in the Edge Spectra with Changes in Ligation 194
5.3.2.3. Pre-edge Feature 194
5.3.2.4. Comparisons with Hydroxylase Edge Spectra 196
5.4. Conclusions 198
5.5. Acknowledgements 199
5.6. References and Notes 200

Chapter 6 Sulfur and Chlorine K-Edge X-ray Absorption Spectroscopic Studies of Photographic Materials 202

6.1. Introduction 203
6.2. Experimental 205
6.2.1. Single-Crystal Polarized Studies 221
6.2.2. Polarized Surface Measurements 222
6.3. Results 224
6.3.1. S K-Edge Spectra of Dye Molecules 224
6.3.1.1. Cyanine Dye Molecules 224
6.3.1.2. Merocyanine Dye Molecules 227
6.3.2. Cl K-Edge Spectra of Dye Molecules 234
6.3.3. Au and Ag Complexes with Sulfur-Containing Ligands 237
6.3.4. Surface Measurements 243
6.4. Discussion 250
6.5. Conclusions 255
6.6. Acknowledgements 255
6.7. References and Notes 256

List of Tables

Chapter 2

Table 2.1. Sample and Data Collection Summary 29
Table 2.2. Results of First Shell Fits to the Hydroxylase Data 37
Table 2.3. Results of Second Shell Fits to the Hydroxylase Data 41
Table 2.4. Iron Fits to Second Shell Data for Oxidized and Semimet Hydroxylase Samples 43
Table 2.5. Results of Wide Shell Fits to the Hydroxylase Data 46
Table 2.6. Results of Fits to the Non-Filtered Hydroxylase EXAFS 51

Chapter 3

Table 3.1. Sample and Data Collection Summary 69
Table 3.2. Results of First Shell Fits to the Hydroxylase Data 77
Table 3.3. Results of Second Shell Fits to the Hydroxylase Data 84
Table 3.4. Results of Wide Shell Fits to the Hydroxylase Data 90
Table 3.5. Results of Fits to the Non-Filtered Hydroxylase EXAFS 97
Table 3.6. Comparison of the Results of Fits to the Hydroxylase Data 111

Chapter 4

Table 4.1. Summary of Information for Dinuclear and Mononuclear Model Compounds 125
Table 4.2. Results of First Shell Fits to the Model Data 138
Table 4.3. A Comparison of the Average First Shell Distances by EXAFS and Crystallography 145
Table 4.4. Fits to Second Shell Model Data 146
Table 4.5. Fits to Second Shell Model Data with Fe and C 155
Table 4.6. Fits to Second Shell Hydroxylase Data 159
Table 4.7. Average First Shell Distances as a Function of First Shell Ligation 163

Chapter 5

Table 5.1. Summary of Samples 178

Table 5.2. Energies of Features in XANES Spectra of Diiron Models 181
Table 5.3. Comparison of Average First Shell Distance with Edge Position 191

Chapter 6

Table 6.1. Energies of Transitions in S K-Edge Spectra of Cyanine Dyes and Dye Intermediates 206
Table 6.2. Energies of Transitions in S K-Edge Spectra of Compounds Containing Exocyclic S 209
Table 6.3. Energies of Transitions in Cl K-Edge Spectra of Dyes and Dye Intermediates 214
Table 6.4 Energies of Transitions in Silver- and Gold-Sulfur Complexes 218

List of Figures

Chapter 1

Figure 1.1. An Fe K-Edge X-ray Absorption Spectrum 10

Chapter 2

Figure 2.1. EXAFS Data of the Hydroyxlase of MMO 32
Figure 2.2. Fourier Transforms of the Hydroyxlase EXAFS Data 33
Figure 2.3. A Comparison of EXAFS Data of Hydroxylase and Model Samples 34
Figure 2.4. The Edge Positions of Diferric, Semimet and Diferrous Hydroxylase Samples 36
Figure 2.5. Fits to Oxidized Hydroxylase Second Shell Data with Iron 44
Figure 2.6. Fits to the Fourier Filtered Oxidized Hydroxylase Data 48
Figure 2.7. Fits to the Fourier Filtered Semimet and Reduced Hydroxylase Data 49
Figure 2.8. A Comparison of Fourier Filtered Second Shell Fe and C EXAFS 54

Chapter 3

Figure 3.1. EXAFS of Semimet Hydroxylase Samples 71
Figure 3.2. Fourier Transforms of the Semimet Hydroxylase EXAFS 72
Figure 3.3. EXAFS of Reduced Hydroxylase Samples 74
Figure 3.4. Fourier Transforms of the Reduced Hydroxylase EXAFS 75
Figure 3.5. Fourier Transforms of Second Shell Fits to Semimet Hydroxylase Data 88
Figure 3.6. Fits to the Non-Filtered EXAFS data for Semimet Hydroxylase Sample 92
Figure 3.7. Comparison of First Shell EXAFS Data for Semimet Hydroxylase Samples 94
Figure 3.8. Comparison of Second Shell EXAFS Data for Semimet Hydroxylase Samples 95
Figure 3.9. Comparison of Interaction Between First and Second Shell EXAFS Data 96
Figure 3.10. Fits to Non-Filtered Semimet Hydroxylase EXAFS Data 100
Figure 3.11. Fourier Transforms of Fits to Non-Filtered Semimet Hydroxylase

EXAFS Data 101
Figure 3.12. Fits to Non-Filtered Reduced Hydroxylase EXAFS Data 103
Figure 3.13. Fourier Transforms of Fits to Non-Filtered Reduced Hydroxylase EXAFS Data 104
Figure 3.14. Edge Spectra of Semimet Hydroxylase Samples 105
Figure 3.15. Comparison of Semimet and Reduced Hydroxylase Edge Spectra 106
Figure 3.16. Edge Spectra of Reduced Hydroxylase Samples 108
Figure 3.17. Comparison of Fourier Transforms of Fe Model and Brominated Derivative 114

Chapter 4

Figure 4.1. EXAFS of Tribridged Model Compounds 132
Figure 4.2. EXAFS of Dibridged Model Compounds 133
Figure 4.3. EXAFS of Monomeric Model Compounds 134
Figure 4.4. Fourier Transforms of Tribridged Model EXAFS 135
Figure 4.5. Fourier Transforms of Dibridged Model EXAFS 136
Figure 4.6. Fourier Transforms of Monomeric Model EXAFS 137
Figure 4.7. Fits to the First Shell EXAFS Data of **FEHBPZOH** 142
Figure 4.8. Comparison of Model-Dependent Fits to Second Shell EXAFS Data 150
Figure 4.9. Comparison of Second Shell EXAFS Data 151
Figure 4.10. Fits to the Second Shell EXAFS Data of **FE2CO2** 153
Figure 4.11. Fits to the Second Shell EXAFS Data of Oxidized Hydroxylase Sample 160
Figure 4.12. Comparison of Average First Shell Distance with O and N Ligation 164

Chapter 5

Figure 5.1. Fe K-Edge XANES Spectra of Oxo-Bridged Model Compounds 183
Figure 5.2. Pre-Edge Features of Iron Model Compounds 184
Figure 5.3. Fe K-Edge XANES Spectra of Non-Oxo-Bridged Model Compounds 186
Figure 5.4. Changes in Edge Spectra with Change in Iron Oxidation State 188
Figure 5.5. Changes in Pre-Edge Feature with Change in Iron Oxidation State 189
Figure 5.6. Comparison of Average First Shell Distance with Position of Edge 192

Figure 5.7. Comparison of Oxidized Hydroxylase Edge Spectrum with Model Spectra 193
Figure 5.8. Comparison of Pre-Edge Feature of Hydroxylase Samples with Model Compounds 197

Chapter 6

Figure 6.1. Schematic of Surface Measurement Geometry 223
Figure 6.2. S K-Edge Spectra of Cyanine Dyes and Dye Intermediates 225
Figure 6.3. Single-Crystal Polarized S K-Edge Spectra of a Cyanine Dye Molecule 226
Figure 6.4. S K-Edge Spectra of Merocyanine Dyes and Dye Intermediates 228
Figure 6.5. Single-Crystal Polarized S K-Edge Spectra of a Merocyanine Dye Molecule 230
Figure 6.6. Comparison of Edge Spectra of Cyanine and Merocyanine Dye Molecules 231
Figure 6.7. S K-Edge Spectra of Thioureas, Mercaptotetrazoles and Mercaptotriazoles 232
Figure 6.8. Comparison of Edge Spectra of Molecules Containing a Thione, Thiol, and Thiolate Exocyclic S 233
Figure 6.9. Cl K-Edge Spectra of Dyes and Dye Intermediates 235
Figure 6.10. Single-Crystal Polarized Cl K-Edge Spectra 9,10-Dichloroanthracene 236
Figure 6.11. S K-Edge Spectra of Silver-Sulfur Complexes 238
Figure 6.12. S K-Edge Spectra of Gold-Sulfur Complexes 239
Figure 6.13. S K-Edge Spectra of Silver and Gold Sulfides 241
Figure 6.14. Single-Crystal Polarized S K-Edge Spectra of a Silver-Sulfur Compound 242
Figure 6.15. The Effect of Ionic and Covalent Metal Interactions on S K-Edge Spectra 244
Figure 6.16. Surface S K-Edge Spectrum of AgBr Sheet Crystal Treated with a Cyanine Dye 245
Figure 6.17. Surface S K-Edge Spectra of AgBr Sheet Crystal Treated with a Merocyanine Dye 247
Figure 6.18. Surface Cl K-Edge Spectra of AgBr Sheet Crystal Treated with a Cyanine Dye 248
Figure 6.19. Surface Cl K-Edge Spectra of AgBr Sheet Crystal Treated with a

Merocyanine Dye 249
Figure 6.20. Surface S K-Edge Spectra of Chemically Sensitized AgBr Sheet Crystals 251
Figure 6.21. Changes in the Appearance of the S K-Edge Spectra with Changing Electronegativity of Substituents 253

List of Abbreviations

acac	acetylacetonate (2,4-pentanedionate)
BIPhMe	2,2'-bis(1-methylimidazolyl)phenylmethoxymethane
Chel	4-hydroxo-2,6-pyridinedicarboxylate
Dipic	2,6-pyridinedicarboxylate
EXAFS	extended X-ray absorption fine structure
$HB(pz)_3$	$[tri\text{-}1\text{-}pyrazolylborate]^{1-}$
Hr	hemerythrin
MMO	methane monooxygenase
PAP	purple acid phosphatase
RR	ribonucleotide reductase
RRB2	ribonucleotide reductase, subunit B2
salmp	$[2\text{-}bis(salicylideneamino)methylphenolate]^{3-}$
TPA	tris(2-pyridylmethyl)amine
Uf	uteroferrin
XANES	X-ray near edge structure
XAS	X-ray absorption spectroscopy

Chapter 1

Introduction to the Methane Monooxygenase Enzyme System and the EXAFS Analysis Method

1.1. Scope and Organization of this Dissertation

This dissertation focuses on the results of experiments conducted over the past 5 years to characterize the dinuclear iron site in the hydroxylase of soluble methane monooxygenase (MMO) from *Methylococcus capsulatus* (Bath). This work has been the result of an extensive and productive collaboration with the group of Prof. Stephen J. Lippard at the Massachusettes Institute of Technology, although very early on, Prof. Howard Dalton's group at the University of Warwick in England provided hydroxylase samples. The MIT group was responsible for isolation and purification of the hydroxylase component from *Methylococcus capsulatus* (Bath), and the early part of their effort focused on improving the purification procedure developed by the Warwick group. All of the hydroxylase samples discussed in this thesis were prepared by the MIT group, as were some of the model compounds which were indispensible to the analysis of the protein data. In addition, the MIT group characterized the hydroxylase by spectroscopic techniques other than X-ray absorption spectroscopy (XAS). The results of these early accomplishments have been published[1] and the non-XAS results will not be discussed in this thesis. More recently, the collaboration has focused on characterizing the interaction between the hydroxylase, the regulatory protein of the MMO system, and substrate.

Only the results as obtained by X-ray absorption spectroscopy will be presented. Each of the experimental chapters will have a brief introduction focusing specifically on the aspect of the project to be discussed. A more general introduction to the methane monooxygenase enzyme system is presented in Chapter 1, along with a discussion of the EXAFS technique and the data reduction and analysis method employed. The EXAFS analysis of the MMO hydroxylase in its three oxidation states is presented in Chaper 2. Chapter 3 discusses the EXAFS analysis of the hydroxylase in the presence of substrate and the regulatory protein of the MMO system. A detailed investigation of the analysis method applied to structurally-characterized dinuclear iron model compounds is presented in Chapter 4. In Chapter 5, the relationship between the structure of the model compounds and the appearance of the edge spectra is examined.

In addition to the biological work described above, a materials project was undertaken as a collaboration with Dr. Teresa A. Smith of Eastman Kodak Company. X-ray absorption spectroscopy was used to characterize the sulfur and chlorine centers in photographic materials. The interaction between S in these materials and Ag and Au metals was also characterized using XAS. The project included single-crystal polarized studies as well as surface measurements using a glancing-angle configuration. The last chapter of this dissertation presents the results of these investigations.

1.2. Methanotrophic Bacteria

Methane is used by methanotrophic bacteria as their primary and sometimes sole source of carbon for growth and energy.[2] Methanotrophic bacteria are found in close association with populations of methanogenic bacteria, which are anaerobic organisms that produce methane as a waste product of their metabolism. The overall oxidation of methane to carbon dioxide is achieved in a series of enzyme-catalyzed reactions, however the first and most difficult step in this pathway is the insertion of an oxygen atom from dioxygen into a C-H bond of methane yielding methanol (eq. 1). This initial oxidation uses NADH as the source of electrons, and is catalyzed by the enzyme system methane monooxygenase (MMO).

$$CH_4 + O_2 + NADH + H^+ \xrightarrow{MMO} CH_3OH + H_2O + NAD^+ \qquad (1)$$

The next step in the oxidation pathway is the conversion of methanol to formaldehyde via methanol dehydrogenase. Formaldehyde is then either used as a source of carbon for cellular biomass, or as a source of cellular energy by further oxidation to CO_2,[3] which generates the NADH required for methane oxidation.

Methanotrophs are classified according to the pathway used to assimilate carbon from formaldehyde into biomass.[3] Type I methanotrophs use the ribulose monophosphate pathway (RMP) in which formaldehyde is condensed with ribose 5-phosphate to eventually yield triose phosphate. Type II methanotrophs use the serine pathway, producing serine from the condensation of glycine with the formaldehyde-derived methylenetetrahydrofolate. In addition to the utilization of different carbon assimilation pathways, Type I and Type II methanothrophs exhibit different intracytoplasmic membrane structures. Type I methanotrophs possess uniformly distributed arrays of stacked membranes, whereas Type II methanotrophs possess paired peripheral membranes. The differences in the membrane structure has been assumed to be correlated to differences in the initial metabolism of methane, however the methane monooxygenase enzyme system is responsible for the initiation of methane utilization for both Type I and Type II methanotrophs.[3]

Methane monooxygenase activity is associated with the cellular membranes of methanotrophic bacteria for all methanotrophs, and with the soluble fractions of cell-free extracts for some Type I and Type II methanotrophs.[4] The availability of copper in the growth media was shown to trigger a switch in the cellular location of monooxygenase activity.[5] As the concentration of copper in the growth media increased from 1 μM to 5

μM, a change from soluble to particulate MMO was detected in cultures of type II methanotroph *Methylosinus trichosporium* (OB3b) and type I methanotroph *Methylococcus capsulatus* (Bath).[6] In addition, oxygen limitation is believed to play a role in the cellular location. It is interesting to note that increasing the concentration of copper (and oxygen) also causes an increase in the amount of intracytoplasmic membrane structure.[7] It is not entirely clear if the presence of copper induces the particulate form of MMO which in turn causes the increase in membrane content, or if the increase in membrane content induces expression of particulate MMO. The particulate form of MMO does contain a copper protein, and the activity of particulate MMO fractions can be increased by the addition of copper salts. Particulate MMO has not been as well-characterized as the soluble form of MMO, but it is currently the subject of many ongoing investigations.[8]

The soluble and particulate forms of MMO differ in almost every way except for their monooxygenase activity. The particulate MMO system consists of a CO-binding cytochrome *c*, a copper-containing protein and a small protein which has not been well characterized,[9] while the soluble MMO system consists of an Fe_2S_2-flavoprotein, a dinuclear non-heme iron protein, and a small regulatory protein.[10] Soluble MMO requires NADH (or NADPH) as a source of electrons for methane oxidation,[11] but electrons from ascorbate or NADH, or from the methanol/formaldehyde dehydrogenase pathways can be utilized by the particulate enzyme system.[9] Particulate MMO activity is sensitive to inhibiting agents such as metal chelators, electron transport inhibitors and other molecules,[9] whereas only 8-hydroxyquinoline and acetylene inhibit the soluble system.[12]

Particulate and soluble MMO from Type I and Type II organisms are non-specific enzyme systems, and catalyze the oxidation of a wide variety of compounds in addition to methane. Some of these compounds are used as alternate growth substrates, and some are cometabolized during oxidation of the primary growth substrate. The soluble MMO system is capable of catalyzing the oxidation of alkanes, alkenes, alcohols, aromatic and alicyclic hydrocarbons, amines and chlorinated hydrocarbons.[13] This lack of specificity is similar to that found in cytochrome P-450[14] and is a trait which enables the methanotrophic bacteria to adapt to changing environmental conditions. The particulate MMO system is not capable of oxidizing as wide a variety of substrates as the soluble system, and is limited to alkenes with 5 carbons or less (the limitation for soluble MMO is 8 carbons) and cannot oxidize alicyclic or aromatic compounds.[5c] In addition, the products of oxidation are somewhat different, with the n-alkanes being oxidized to primary and secondary alcohols by the soluble system, while only secondary alcohols result from particulate MMO oxidation.

The mechanism of oxidation for the soluble MMO system has been studied by identifying the products of oxidation for a variety of substrates. Loss of stereochemistry for the oxidation of *cis*-1,4- and *cis*-1,3-dimethycyclohexane, allylic rearrangements observed in methylene cyclohexane oxidation, the NIH shift observed for aromatic hydroxylation and the opening of cyclopropyl rings all suggest a non-concerted reaction mechanism of hydrogen abstraction followed by hydroxylation proceeding via carbocation or radical intermediates.[15] A large kinetic isotope effect has been reported for the oxidation of methane, suggesting that breaking the C-H bond is rate-limiting.[16]

The soluble form of MMO has been the focus of much of the research of monooxygenase activity because of its broader substrate specificity and the greater ease of isolation and purification of soluble extracts of MMO as compared to membrane-bound forms. In general, however, the ability of MMO to catalyze the oxidation of methane to methanol has generated interest in this enzyme system, or in models of this enzyme system, as a biocatalyst for methane conversion and alkane oxidation.[17] A more recent interest in the methanotrophic bacteria from which MMO is isolated concerns the ability of MMO to catalyze the oxidation of halogenated hydrocarbons. Trichloroethylene (TCE) is a source of considerable groundwater pollution and a suspected carcinogen.[18] The byproducts of the naturally occurring anaerobic degradation of TCE (via reductive dehalogenation) are even more recalcitrant to anaerobic processes, and vinyl chloride, a known carcinogen, accumulates in anaerobic TCE-contaminated aquifers.[19] Under aerobic conditions, the degradation of TCE occurs readily, and the susceptibility of the byproducts to aerobic degradation is greater than that of TCE.[20] TCE is not a growth substrate for methanotrophs, however at low concentrations, TCE is cometabolized by methanotrophic populations grown on methane (high concentrations of TCE is toxic to methanotrophs). The rate and extent of TCE oxidation depends on a number of factors, including growth conditions and availability of reducing power for the catabolic process.[21] With the proper approach, however, undesirable solvents in groundwater supplies can be cometabilized by methanotrophic populations.[22]

1.3. The Soluble Methane Monooxygenase Enzyme System

Soluble methane monooxygenase has been isolated and purified from Type I methanotroph *Methylococcus capsulatus* (Bath),[10a,11a] and Type II methanotrophs *Methylosinus trichosporium* (OB3b)[10c,12] and *Methylobacterium* sp. Strain CRL-26.[10b] MMO from *M. capsulatus* (Bath) and *M. trichosporium* (OB3b) was resolved into three components consisting of a hydroxylase, a reductase and a small regulatory protein

(component B). The soluble MMO system from *Methylobacterium* sp. Strain CRL-26 was resolved into only two components, the hydroxylase and the reductase. The hydroxylase component[10c,23] (M_r 250 kDa) consists of three polypeptide subunits in an $\alpha_2\beta_2\gamma_2$ arrangement and contains 2-4 non-heme iron atoms per protein unit depending on conditions of growth, harvesting and purification. EPR studies of the hydroxylase component from *M. capsulatus* (Bath) have suggested that the protein is a non-heme dinuclear iron protein.[24] The reductase component[25] (M_r 39 kDa) contains one FAD and one Fe_2S_2 cluster, while the regulatory protein[26] (M_r 16 kDa) contains no metal atoms or prosthetic groups. All three protein components are required for efficient oxidation of substrate for the MMO enzyme systems from both *M. capsulatus* (Bath) and *M. trichosporium.* (OB3b). The reductase from *M. capsulatus* (Bath) and *Methylobacterium* sp. CRL-26 are essentially identical, giving rise to the same absorption spectrum (band at ~ 460 nm with a shoulder at 395 nm), EPR spectrum (rhombic with g values of 1.86, 1.96, 2.04 typical of an Fe_2S_2 center) and redox potentials (-247, -195, -250 mV for the Fe_2S_2, FAD/FADH, FAD/$FADH_2$ couples from *Methylobacterium* sp. CRL-26; -220, -150, -260 mV for the same couples from *M. capsulatus* (Bath)).[25]

The reductase component from *M. capsulatus* (Bath) rapidly accepts electrons from the NADH and transfers those electrons to the hydroxylase component.[27] Studies of the oxidation of NADH by apo-Fe_2S_2 and apo-Fe_2S_2·apo-FAD reductase demonstrated that the FAD center interacts directly with NADH accepting 2 electrons. These electrons are transferred one at a time to the Fe_2S_2 center, which can carry only one electron,[28] and it is the Fe_2S_2 center which interacts with the hydroxylase component relaying single constant-potential electrons. Intermolecular transfer of electrons from NADH to the hydroxylase via the reductase occurs in the presence or absence of substrate.

EPR studies of the hydroxylase component in the presence of ethene and cyanomethane, in which the EPR spectra sharpened and increased in intensity, suggested that the hydroxylase interacted directly with the substrate.[29] Studies with a high specific-activity form of the hydroxylase from *M. trichosporium* (OB3b) have shown that in the absence of reductase and component B, single turnover is achieved when the hydroxylase is reduced to the diferrous form non-enzymatically and exposed to dioxygen.[30] This confirms that the hydroxylase component contains the site where substrate binding and oxidation occur, and the 2 e^- reduced form of the hydroxylase is the catalytically important state. While there is little doubt about the role of the reductase and hydroxylase component, there is some question about the role of component B in the substrate oxidation process.

As noted above, electron transfer between the reductase and the hydroxylase occurs in the absence or presence of substrate for the *M. capsulatus* (Bath) enzyme system, resulting in the reduction of O_2 to H_2O. Substrate oxidation did not occur unless component B was present.[27] In the absence of substrate and the presence of component B, electron transfer between the hydroxylase and the reductase decreased dramatically, or no longer occurred. This suggests that component B serves to convert the hydroxylase from an oxidase to an oxygenase by regulating the transfer of electrons from the reductase to the hydroxylase to the presence of oxidizable substrate, perhaps as a conservation mechanism for reducing equivalents. In contrast, oxidation products were detected for a system consisting of a high specific-activity hydroxylase of MMO from *M. trichosporium* (OB3b), O_2, NADH and reductase, with no component B present.[30] This difference in the role of component B as a requirement for substrate oxidation could reflect a true difference in the mechanism of oxidation for the MMO complex from the two types of methanotrophs, or the difference in the activity of the hydroxylase as isolated from *M. trichosporium* (OB3b), or the differences may arise from the different relative concentrations of the various proteins used to execute the studies. As noted above, the MMO system from *Methylobacterium* sp. Strain CRL-26 consists of only the hydroxylase and reductase, hence these three species could reflect specializations in the development of the MMO system in response to specific environmental conditions.

Component B interacts with the α subunit of the hydroxylase, while the reductase interacts with the β subunit.[31] The presence of B perturbs the EPR spectrum of the hydroxylase. In addition, the distribution of the oxidation products of the hydroxylation reaction was found to change when B was present.[32] The interaction of the components of the MMO enzyme system therefore has an effect on the diiron site in the hydroxylase component. Understanding the nature of the change at the iron center is an important step in developing an understanding of the mechanism of oxygen activation.

1.4. Spectroscopic Studies of Dinuclear Non-Heme Iron Centers

EPR studies of the hydroxylase component of soluble MMO[24] have suggested that this protein belongs to the class of dinuclear non-heme iron proteins which includes hemerythrin (Hr), ribonucleotide reductase subunit B2 (RRB2), purple acid phosphatase from beef spleen (PAP) and uteroferrin from porcine uterine linings (Uf).[33] These proteins serve very different functions: hemerythrin is an oxygen transport protein, ribonucleotide reductase converts ribonucleotide diphosphate to deoxyribonucleotide diphosphate for DNA synthesis, the purple acid phosphatases hydrolyzes phosphate esters, and methane

monooxygenase is an oxygen activation protein; however, they have many similar spectroscopic features[33] suggesting that they have similar active site structures as well. Understanding the structural basis of the spectroscopic similarities and functional differences of these protein systems has been a major focus of research in a number of laboratories.

Structurally characterized inorganic model compounds which mimic the spectroscopic and/or catalytic properties of the dinuclear non-heme iron protein active site are an important tool in understanding structure-function relationships in these protein systems. As a result, a number of multiply bridged non-heme iron models have been synthesized and spectroscopically characterized, and Kurtz has published an extensive review of the models of dinuclear non-heme iron sites.[34] These models are di- or tribridged with either an oxygen atom (oxo-bridge) or a hydroxide group (hydroxo-bridge) as one of the bridging units, with the balance of the bridges being made up of carboxylate, alkoxo, or hydroxo groups.[35] The dominant structural feature of these model compounds is the presence (or absence) of a μ-oxo bridge between the iron atoms ($Fe\text{-}O_{oxo}$ distance of ~ 1.8 Å; $Fe\text{-}O_{hydroxo}$ distance ~ 2.0 Å), which imparts characteristic spectroscopic features. The Fe-O-Fe unit gives rise to strong electronic absorption bands between 300 - 400 nm, which have been assigned as ligand-to-metal (oxo-to-iron) charge transfer transitions,[36] and a pair of weak bands between 440 - 510 nm, attributed to ligand field transitions which gain intensity by mixing of oxo-to-iron charge transfer transitions.[37] Hydroxo-bridged models have relatively featureless electronic absorption spectra. The symmetric vibrational stretch of the Fe-O-Fe occurs between 380 and 450 cm^{-1}, and the asymmetric stretch between 725 and 885 cm^{-1}. The hydroxylase of methane monooxygenase exhibits none of these absorption bands.[1] The Fe-OH-Fe stretch is reported to occur between 3400 and 3600 cm^{-1}.

Diferric oxo- and hydroxo-bridged models exhibit isomer shifts in the range of 0.35-0.60 mm/s by Mössbauer spectroscopy, characteristic of 5- or 6-coordinate high-spin iron atoms (S = 5/2 ground state). Quadrupole splittings (ΔE_Q) greater than 1 are characteristic of the presence of an oxo-bridge; hydroxo-bridged models have quadrupole splittings < 1. Magnetic susceptibility measurements indicate that in almost every case, the diferric iron atoms exhibit antiferromagnetic coupling ($J < 0$). Values of the coupling constant, J, for oxo-bridged compounds are in the range of 80 to 120 cm^{-1}, while hydroxo-bridge models have coupling constants in the 7 to 17 cm^{-1} range. The coupling constant for the semimet hydroxylase has been determined to be $J = -32$ cm^{-1}.[1] The large difference in the magnitude of J is an indication of the ability of the oxo-bridge to mediate strong spin-exchange coupling in these systems, and therefore of the involvement of oxo-bridge

orbitals in a superexchange pathway between the iron atoms. The presence of the other bridges in the center has little effect on the magnitude of J, and therefore play a negligible role in the spin-exhange coupling. A correlation has been shown to exist between the magnitude of the coupling constant, J, and the shortest superexchange pathway in the molecule, which in every case would involve only the short Fe-oxo bridge (Fe-O_{oxo} distance ~ 1.8 Å) instead of the longer Fe-carboxylato bridge (Fe-$O_{carboxy}$ distance ~ 2.0 Å).[38]

The diferric forms of Hr, RRB2, Uf, and MMO consist of 5- or 6-coordinate high-spin iron atoms which are antiferromagnetically coupled. All of the proteins mentioned above have been structurally characterized by X-ray absorption spectroscopy,[39] and Hr and RR have been characterized by crystallography as well.[40] These studies have shown that the iron active sites of these proteins have in common octahedrally-coordinated high spin iron atoms which are antiferromagnetically coupled. Hr has a (μ-oxo)bis(μ-carboxylato) tribridged diiron core, an open coordination site for dioxygen binding and N ligation from histidines (total of 5 histidine groups) completing the coordination sphere.[40a,b] The RR diiron center has a (μ-oxo)(μ-carboxylato) dibridged iron core with only two histidine atoms coordinating and the rest of the coordination sphere consisting of O-donating carboxylate groups.[40c] The iron core in Uf is suggested based on EXAFS analysis to also be dibridged, but no evidence for an oxo-bridge was found. Instead, a (μ-hydroxo/alkoxo)(μ-carboxylato) core is suggested for the Uf active site.

The differences in the structures of the dinuclear iron centers of the proteins described above contribute to the different roles they serve. The characterization of the active site of MMO using X-ray absorption spectroscopy will provide additional information about the variations in the structure of dinuclear iron centers in biology which lead to different functions.

1.5. X-ray Absorption Spectroscopy

X-ray absorption spectroscopy (XAS) involves the measurement of the absorption coefficient, μ, of an element of interest as a function of energy (eV). Sharp discontinuities in the absorption coefficient, called edges, arise when a photon is absorbed with energy equal to the ionization energy of an electron in the absorbing species. The X-ray edges are named according to the Bohr atomic level from which the photoionized electron originates. For example, a K-edge refers to the ionization of a 1s electron. The spectrum obtained in an XAS experiment is divided into three regions (Figure 1.1). The structure in the edge region, sometimes referred to as the X-ray absorption near-edge structure (XANES),

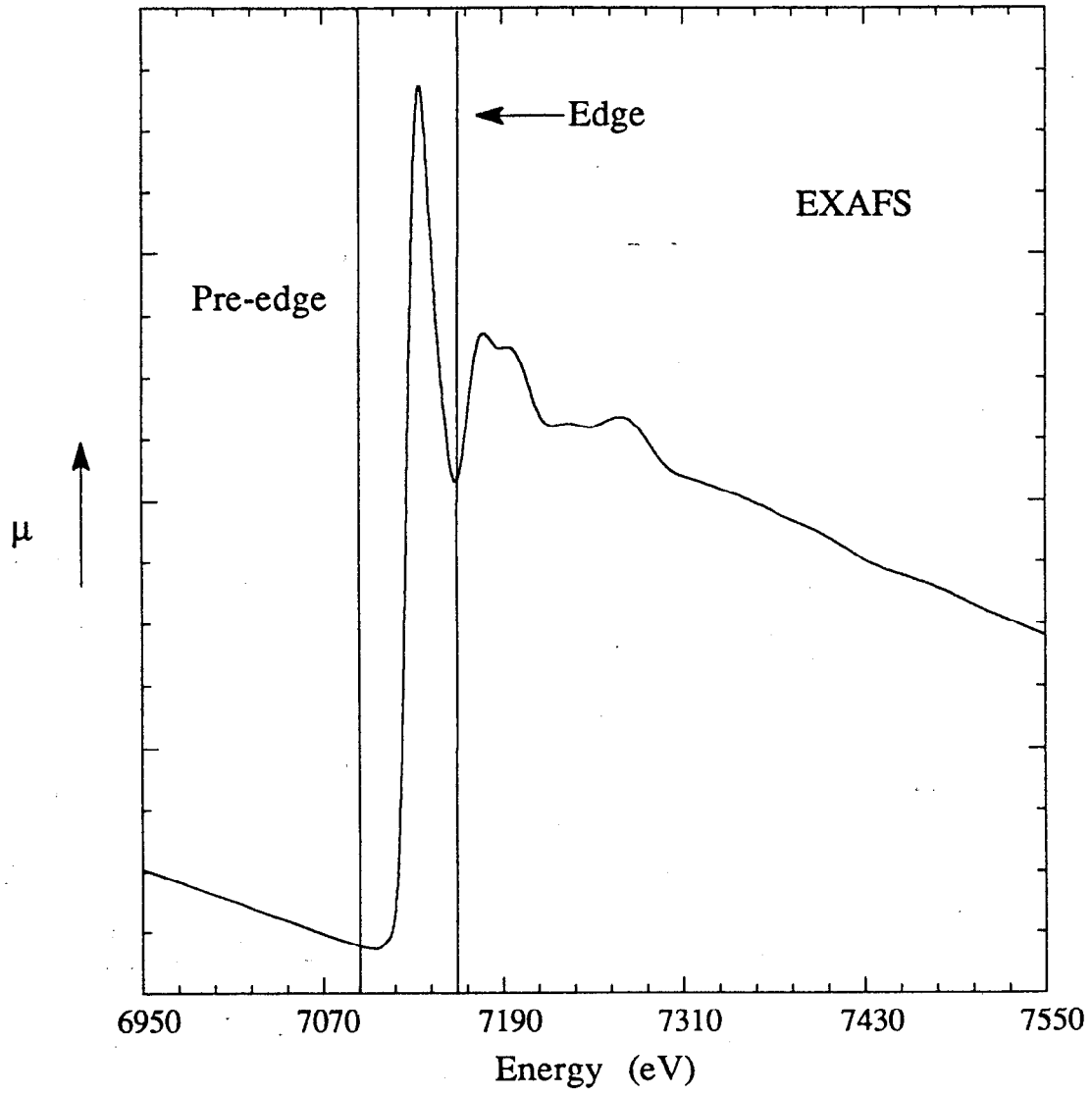

Figure 1.1. An Fe K-edge X-ray absorption spectrum. μ is the absorption coefficient. The data were measured in transmission mode. The slope in the pre-edge and EXAFS region is the background caused by the absorption of lower Z atoms in the sample, as well as by absorption from air, tape and windows.

contains information about the electronic structure of the absorbing atom. Above the edge region, the modulation in the absorption coefficient is referred to as the extended X-ray absorption fine structure (EXAFS) and contains information about the local geometric structure of an absorbing atom.[41] The absorption edges for most biologically relevant transition metal ions are accessible with the current X-ray sources available, but the use of high-intensity synchrotron radiation over a broad range of energies has been essential for the application of XAS to the study of dilute metalloprotein samples.

XAS has proven itself to be a valuable probe of the active site of metalloproteins[42] because it specifically probes the environment around the metal center and can be used on non-crystalline samples of dilute metalloproteins. The X-ray absorption edge region contains transitions to bound atomic and molecular states localized on the absorbing atom, as well as to localized and delocalized continuum resonances.[43] The position of the edge is directly related to the oxidation state of the absorbing atom, and variations in the position of the edge features among samples in the same oxidation state therefore reflect changes in the covalency of the metal site. In addition, the appearance of the edge is indicative of the coordination number and site symmetry of an absorbing atom. The analysis of the edge structure of dinuclear iron systems will be presented in Chapter 5 along with a more detailed discussion of the interpretation of XANES (X-ray absorption near edge structure) data.

Above the edge region, the photoelectron is ejected into the continuum. Analysis of the modulation pattern of the data in this region produced by backscattering of the X-ray excited photon from neighboring atoms gives information about the type, number and distances of nearest neighbors to the absorbing atom.[44] The edge thresholds for first row transition metals are separated by several hundred eV, which allows specific information about different metal-containing sites within a single protein to be obtained. The theory and use of EXAFS, and a description of the data reduction and analysis technique are presented below. Details of the design and execution of an EXAFS experiment have been extensively reviewed[44,45] and will not be presented here.

1.5.1. Extended X-ray Absorption Fine Structure

EXAFS analysis gives information about the average local structural environment of an absorbing atom. The modulations in the absorption coefficient result from a scattering process involving the neighboring atoms and therefore depend on the coordination environment of the absorbing atom. The analysis below considers only the single scattering interaction between the photoelectron and neighboring atoms. Single

scattering describes the process in which the photoelectron propagates away from the absorbing atom, scatters off of a neighboring atom, and travels directly back to the absorbing atom The standard EXAFS equation for the K-edge and single scattering is given by:[46]

$$\chi(k) = \sum_{S} N_s \frac{|f_s(\pi,k)|}{kR_{as}^2} \exp(-2\sigma_{as}^2 k^2) \exp\left(\frac{-2R_{as}}{\lambda}\right) \sin[2kR_{as} + \alpha_{as}(k)] \qquad (2)$$

where N_S is the number of scattering atoms at an average distance R_{as} from the absorbing atom. $|f_s(\pi,k)|$ is the backscattering amplitude and $\alpha_{as}(k)$ is the phase shift of the scattering atom; both are dependent on backscattering atom type. λ is the mean free path which accounts for the finite lifetime of the photoelectron, and k is the photoelectron wavevector, given by equation 3, below. The Debye-Waller factor, $\exp(-2k^2\sigma^2_{as})$ accounts for thermal and/or structural disorder in a given coordination sphere, with σ_{as} defined as the root-mean-square variation of atomic distances from the average R_{as}. The EXAFS for any absorbing atom/scattering atom pair can be represented as a damped sine wave with amplitude ($[N_s|f_s(\pi,k)|\exp(-2\sigma^2_{as}k^2)\exp(-R_{as}/\lambda)]/[k(R^2_{as})]$), frequency ($2R_{as}$) and phase shift ($\alpha_{as}(k)$) characteristic of the atoms involved. The total EXAFS is given by the summation of the individual sine waves which describe each absorbing atom/scattering atom interaction. The modulation of the absorption coefficient is therefore the interference pattern resulting from the superposition of the various sine waves originating from the interaction of the photoelectron with neighboring atoms, as measured at the location of the absorbing atom. The frequency of the EXAFS contains information about the distance to neighboring atoms, the amplitude has information about the numbers of neighboring atoms, and information about the types of scattering atoms can be obtained from both the amplitude and phase of the EXAFS. Analysis of the EXAFS data therefore yields information about the geometric structure of an absorbing atom site.[47]

The amplitude of the EXAFS weakens at higher k due to the $1/k$ dependence of the EXAFS expression, from damping by the exponential Debye-Waller term, and from the lifetime limit represented by the mean free path. This damping effect can be compensated for in the data analysis by k weighting $\chi(k)$. In addition, the backscattering amplitude, $|f_s(\pi,k)|$, describes an amplitude function that is characteristic of the atom type and reaches a maximum at some value of k, representing the region of the EXAFS data to which the atom contributes most significantly. Therefore, k weighting of the data can also increase the relative contribution of atoms which scatter more strongly at higher k values and allow this information to be enhanced in the EXAFS analysis. Among the atoms which

contribute to higher k data are transition metals, therefore the weighting scheme is particularly important for metalloprotein data. Additionally, the single-scattering approximation which is used for the analysis of the EXAFS data is valid at higher k. In all of the analysis presented in this dissertation, the EXAFS analysis is based on k^3-weighted data. This weighting scheme has proven to provide the best compromise between enhancing the contribution of high k data without overemphasizing the increased noise level of the data in the high k region.

As shown above, EXAFS is expressed as a function of k, the photoelectron wave vector, however the absorption data is measured as a function of energy. The relationship between energy and k is given by:

$$k = [2m_e(E - E_0)/\hbar^2]^{1/2} \qquad (3)$$

where m_e is the electron mass, E is the photon energy, $\hbar$ is Planck's constant divided by 2π, and E_0 is the threshold energy, where k is defined to be zero, with units of $Å^{-1}$. The contribution of each shell of atoms to the EXAFS data is represented as a damped sine wave with a frequency and amplitude characteristic of the scattering pair. The individual contributions can be conveniently visualized by performing a Fourier transform on the k^3-weighted EXAFS data (from $Å^{-1}$ to Å space) which results in a peak corresponding to the frequency of each sine wave component in the EXAFS. Since the frequency of the sine wave is directly proportional to the distance between the absorbing and scattering atoms (frequency = $2R_{as}$) the generated Fourier transform represents the radial distribution of atoms around an absorbing atom.

Each peak in the Fourier transform of the EXAFS data corresponds to a shell of coordinating atoms, however the positions of the peaks do not give accurate distance information because of the k-dependent phase shift, $\alpha_{as}(k)$, in equation 2. α_{as} will contribute to the frequency of the sine wave by an amount a_1, where a_1 is the coefficient of the k-weighted term in the expansion of α_{as} (see equation 6, below). The true frequency of the sine wave is then $(2R_{as} + a_1)$ so the position of the peak is shifted from the correct distance R_{as} by an amount $a_1/2$. The magnitude of this phase shift depends on the types of atoms present in the center. Nevertheless, the Fourier transform allows the principal frequency contributions to the EXAFS data to be isolated and independently analyzed which simplifies the initial curve-fitting procedure described in the following section.

The EXAFS amplitude is proportional to $(R_{as})^2$, therefore the same atom at longer distances from the absorbing atom contribute less strongly to the EXAFS than one nearby. EXAFS analysis can therefore yield structural information only within a limited radius of

the absorbing atom. Structural disorder also contributes to the distance limitation of EXAFS analysis by increasing the Debye-Waller term and therefore decreasing the EXAFS amplitude. For dilute metalloprotein systems, structural information within 4 Å is typically accessible by EXAFS. In addition, if an atom is in more than one environment in a sample, the structural information obtained will be an average over all absorbing atom sites.

The above description of the EXAFS does not include the contributions from multiple scattering pathways. These pathways involve angle-dependent scattering of the photoelectron which contribute to outer shell EXAFS data and involve the interaction of the photoelectron with two or more atoms before returning to the absorbing atom. In general, multiple scattering contributions are weaker than single scattering contributions within the same coordination shell, but may be significant compared to single scattering processes involving a more distance shell of atoms. Specifically, multiple scattering pathways may contribute significantly to the second shell data of dinuclear metal systems and therefore interfere with the analysis of the second shell data using the single scattering form of the EXAFS equation described above. Further discussion of the multiple scattering process is presented in Chapter 4. The first shell data will have no contributions from multiple scattering pathways due to the length of the pathways involved. The low k region of the EXAFS data frequently can have dominant contributions from multiple scattering effects and is not included in data analysis in the absence of a theoretical approach.

There are certain experimental considerations that impact the quality of experimental EXAFS data. First and foremost is the signal-to-noise level of the data which is primarily a function of the concentration of the absorbing atom in the samples. The EXAFS signal is weak compared to the absorption edge (often a few percent of the intensity), therefore in an EXAFS analysis, information is being extracted from a weak signal on a large background. As noted above, the EXAFS signal is damped at high k and must therefore be weighted to obtain an equal contribution over the entire k range. However, the noise contribution is also increased by the weighting scheme, and will limit the amount of data available for further analysis, whihc in turn limits the structural information which can be obtained. In addition, the shorter the k range of the data, the less well-resolved are the frequency contributions to the Fourier transform of the EXAFS data, and therefore the EXAFS analysis will not be able to distinguish between shells of atoms in the same coordination sphere at slightly different distances. For example, for data to $k = 14$ Å^{-1}, the differences in the distances of coordinating shells of atoms greater than ~ 0.11 Å can be resolved, but for data to 10 Å^{-1}, the distance differences have to be greater than ~ 0.16 Å. In general, obtaining data to a high k range will improve the resolution of distance contributions within the same shell.

The most effective way to improve the signal-to-noise level is to maximize the concentration of the absorbing species in the sample, sometimes difficult for biological samples due to increasing viscosity of concentrated samples and dangers of precipitating the protein. The signal-to-noise level for dilute systems is improved by collecting numerous scans which are averaged together for further analysis. The quality and range of data is then limited by the amount of time available to collect data on the sample. Additionally, the intensity of the incoming beam is an important factor and use of a wiggler beamline greatly improves the quality of the data compared to a bending magnet beamline.[45] Another factor which limits the range of data available for analysis is the damping of the EXAFS resulting from disorder in the structure. There are two contributions to the Debye-Waller factor, a dynamic and a static term. The static term arises from structural disorder in the sample such as a variety of distances to atoms in the first coordination sphere. The dynamic disorder involves vibrational motion of atoms relative to each other. The vibrational contribution to the Debye-Waller factor can be minimized by collecting data at low temperatures, thereby decreasing the damping of the EXAFS amplitude and improving the quality of the data to some degree. In addition, maintaining biological samples at low temperatures may reduce radiation damage and slow photoreduction of the sample caused by the formation of hydrated electrons in aqueous solutions which react with the metal site.

1.5.2. Data Reduction and Analysis

The initial steps in data reduction involve energy calibration of each scan, inspection and averaging of individual scans, and removal of monochromator glitches if necessary from the averaged data set. These methods are discussed in the experimental sections of following chapters. The more critical steps in the data reduction procedure are background subtraction and normalization which allow the EXAFS to be extracted from the averaged data file.

EXAFS ($\chi(k)$) is defined as the modulation of the absorption coefficient, μ, and can be expressed as:

$$\chi(k) = (\mu - \mu_0)/\mu_0 \qquad (4)$$

where μ_0 is the free-atom absorption coefficient which would be observed if the sample contained only the absorbing atom without any neighboring scattering atom. In equation 4, the EXAFS modulations are isolated from, and normalized to, the free-atom absorption,

effectively yielding information on a per atom basis. In an XAS experiment, the absorption (or fluorescence) measured consists of the absorption coefficient, μ, plus a background contribution, μ_{back}, arising from absorption from lower Z atoms in the sample or scatter from the sample, as well as absorption from windows, tape or air in the beam path. In order to obtain μ from the experiment, the background must be subtracted from the measured data. The absorption background, μ_{back}, decreases monotonically with increasing energy and can be approximated by a polynomial which is fit to the data in either the pre-edge or post-edge region of the spectrum, extrapolated through the rest of the spectrum and subtracted. Alternatively, the absorption of a blank sample containing everything except the absorbing species of interest can be measured and then subtracted from the sample absorption. In practice, creation of an accurate blank is a difficult task, so the polynomial fitting method is typically used. This method does not result in complete removal of the background and will leave some residual background, μ_{res}, in the data which is removed in the next step.

The free-atom absorption, μ_0, cannot be measured and must therefore be approximated in some way. The free-atom absorption would be a smooth curve upon which the EXAFS oscillations are superimposed and can be modeled by a curve obtained by fitting a polynomial spline to the data in the post-edge region. This method will also model and remove μ_{res}, the residual background left from the absorption correction procedure described above. A different value of μ_0 must be used in the denominator of equation 2 to normalize the EXAFS data because the curve will include μ_{res}. The value of μ_0 used for normalization is usually calculated by using the Victoreen formula.[48]

The determination of μ_0 by the spline curve-fitting method is not a trivial task. In general, a three or four region spline is used depending on the range of data available, and the fitting procedure involves changing the lengths of the various regions and the orders of the polynomials used within each region. The criteria which must be matched is that the polynomials must meet at the border of a region with equal value and equal slope. Care must be taken to insure that the curve used to mimic the background does not distort the EXAFS when it is subtracted from the data. This is generally done by monitoring both the appearance of the spline, the EXAFS and the Fourier transform of the EXAFS during the spline-fitting procedure. The curve chosen to represent $\mu_0 + \mu_{res}$ should maximize the intensity of the peaks in the Fourier transfom and minimize the low R noise, and the amplitude of the EXAFS above and below the zero line should show no ultra-low-frequency structure. Improper background subtraction can result in errors in the structural information obtained by EXAFS analysis. Distortion of the EXAFS can be manifested as changes in both the frequency and the amplitude of the data, thereby leading to incorrect

distance and coordination number determinations. For that reason, it is best to use few regions for the spline fitting technique and low orders of polynomial within the regions to prevent excessive curve in the spline. Using nodes in the EXAFS data as the end points of the curve-fitting regions and distributing the regions evenly in *k* space has proven to be a reasonable approach for determining the spline.

The experimental factors which contribute to the background include harmonic contamination of the incident beam, effects from ice in the solution samples, and absorption from low Z atoms in, or scatter from, the sample as mentioned above. These effects can be reduced by using proper experimental technique. Harmonic contamination can be minimized by detuning the monochromator, which very slightly misaligns one of the two monochromator crystals. This results in a decrease in the contribution to the intensity from the higher harmonic reflection relative to the contribution from the primary reflection due to the narrower shape of the higher-harmonic rocking curve. Ice effects, which range from increased noise to diffraction peaks, can be minimized by adding ethylene glycol or glycerol to the buffer/solvent system for solution samples to facilitate the formation of glasses. Alternatively, if ice effects are a problem in the data, thawing and rapidly freezing the sample may reduce the size of the ice crystals, thereby reducing the diffraction effects. The absorption from low Z atoms in the sample for data collected in transmission mode can only be eliminated by the background subtraction method discussed above. In general, transmission measurements are used for concentrated samples, because the signal should be large compared to the background. For dilute samples, the transmitted signal is weak compared to the background, so fluorescence detection is used. In fluorescence mode, contributions to the background from scatter can be reduced by using a filter which absorbs the scatter at energies below the fluorescent signal of interest. The easiest way to achieve this is to make a filter of the element one atomic number lower than the element of interest (Z-1 filter) for first row transition metals. Solid state fluorescence detectors allow electronic windowing of the signal of interest, so that only photons from the appropriate Kα line are detected.[49]

Normalization of the data scales the spectra to give a value of one for the absorption edge and allows the data to be interpreted on a per atom basis. Data for different samples can then be directly compared to one another. The edge region is sensitive to the chemical environment of the absorbing atom, therefore the point at which the data is scaled must lie above the edge region so that the normalization procedure is independent of the nature of the sample. In practice, the data is normalized at E_0, defined as the beginning of the continuum region of the XAS spectrum. The scale factor which is used to normalize the

data corresponds to the difference between the curve fit to the postedge region and the curve used to mimic and remove the absorption background, as measured at E_0.

The first step in extracting metrical information from the normalized, background-subtracted EXAFS is to Fourier transform the k^3-weighted EXAFS data, thereby revealing the phase-shifted radial distribution function. The individual contributions to the EXAFS are isolated from the Fourier transform by applying a window, or filter, to isolate the region of interest in the transform which is then backtransformed into k space for further analysis. Fourier filtering will distort the data somewhat due to artifacts introduced by truncating the data. These effects can be minimized by using a window smoothing function. For that reason, a Gaussian window of width 0.1 Å was used to smooth the window used to isolate the EXAFS data for transformation to R (Å) space, and the peaks in the Fourier transform for backtransformation to k (Å^{-1}) space for curve-fitting analysis.

Analysis of the structural information contained in the EXAFS data involves the simulation of the EXAFS for a hypothetical arrangement of atoms around the absorbing atom. The EXAFS interaction between a given absorbing atom/scattering atom pair is constructed with the use of the appropriate amplitude and phase functions ($|f_s(\pi,k)|$ and $\alpha_{as}(k)$ in equation 2), distances (R_{as}), coordination numbers (N_s), energy shifts (E_0), and Debye-Waller factors (σ^2_{as}). In addition, an amplitude reduction factor may be required. A non-linear least squares curve fitting technique is used fit the hypothetical EXAFS to the data by allowing certain parameters to vary, depending on the method of curve fitting used. Theoretical amplitude and phase functions are tabulated for the plane-wave[50] and curved-wave approximations.[51] These functions often require the use of an amplitude reduction factor and edge shift, ΔE_0, to scale the theoretical amplitude and phase functions. These values are sometimes determined with the aid of structurally characterized models in an approach called FABM, or fine adjustment based on models.[52]

A second approach involves the use of appropriate, structurally characterized models to empirically determine amplitude and phase functions for a given scattering pair,[53] and is the method used for the EXAFS analysis presented in this thesis. The amplitude and phase functions required are parameterized according to:

$$|f_s(\pi,k)| = c_0(\exp[c_1k + c_2k^2]\ k^{c_3} \tag{5}$$

$$\alpha_{as}(k) = \frac{a_{-1}}{k} + a_0 + a_1k + a_2k^2 \tag{6}$$

The values of c_1 and a_{-1} are zero in the work described herein. The method involves fitting the Fourier-filtered EXAFS data for the model compound (to isolate the shell of interest),

using the correct distance and coordination number and optimizing the initial c and a parameters in an iterative method. Initially, all 6 parameters are varied in a fit to the data. The optimized parameters are then used as the starting point for the next iteration by successively allowing just the amplitude or the phase parameters to vary in the fits to the data. Once the sets of amplitude and phase parameters no longer changed during the fits (after 4 cycles), all of the parameters were allowed to vary for the final iteration. These empirically-derived amplitude and phase parameters for a scattering pair are then used to fit the EXAFS of interest by letting the distance and coordination number vary in the fit to the unknown .

Not surprisingly, the choice of the model compound from which to extract the amplitude and phase functions in this manner is critical. The assumption implicit in the use of amplitude and phase parameters as obtained by model compounds is that the parameters describe a generic absorbing atom/scattering atom interaction and are therefore transferable to other models; however, this is not always true. For that reason, models from which the amplitude and phase backscattering parameters are extracted should be chosen based on a reasonable similarity to the unknown. The compound chosen to model the absorbing atom/scattering atom interaction should have an equidistant distribution of only the scattering atom in the coordination shell of interest and the single scattering process should dominate. In general, parameters obtained from a first shell analysis of a model compound are not transferable to the second shell or vice versa. The transferability of the parameters must be tested in fits to other structurally characterized models before fits to an unknown are done. Similar Fourier transform ranges, windows and fitting ranges in both k ($Å^{-1}$) and R (Å) space should be used for extracting empirical parameters from models and fitting the unknown both to minimize truncation artifacts due to the Fourier filtering technique, and because of the k-dependence of the parameters. In addition, data on the models and the unknown should be collected at the same temperature due to the dependence of the amplitude function and Debye-Waller term on temperature.

Non-linear least-squares curve fitting techniques are subject to variable correlation, especially between R_{as} and E_0 and N_s and σ^2_{as}. For that reason, two of the four variables are generally fixed (one from each pair of correlated variables) and the other two are allowed to float during the fitting procedure. The parameters varied in the FABM technique are generally the distance and coordination number or Debye-Waller factor, using a value of E_0 and an amplitude reduction factor from model compounds to calibrate the theoretical phase and amplitude functions, respectively. For the empirical method used here, E_0 and the Debye-Waller factor are fixed and the distance and the coordination number are varied. The Debye-Waller factor is represented by c_2 in the amplitude parameter set and is therefore

determined using model compounds. The determination of E_0 is arbitrary, but the value used consistently for Fe, 7130 eV, has allowed the determination of accurate distances. Using this technique in applications to structurally-characterized model compounds, errors of ± 0.03 Å in the distance determination, and of 25% in the coordination number are estimated.[44,47,49,53]

When using a non-linear least squares fitting technique care must be taken in the interpretation of fit results. It is important to step through distances and coordination numbers in the fitting procedure to insure the identification of a global, rather than a local, minimum corresponding to the best fit. A fitting parameter, F ($F = \{[k^6(\text{data} - \text{fit})^2]/(\text{no. points})\}^{1/2}$) is calculated for each fit attempt and the magnitude of F indicates the "goodness" of the fit with smaller values suggesting a better fit, although one must still inspect the data and the fit and not rely only on the value of F calculated. The fits are not constrained, therefore chemical intuition must be used to evaluate the reasonableness of any fit result. An examination of the application and limitation of the empirical curve-fitting technique in fits to the first and second shell of dinuclear iron model compounds is presented in Chapter 4.

1.6. References and Notes

1. DeWitt, J. G.; Bentsen, J. G.; Rosenzweig, A. C.; Hedman, B.; Green, J.; Pilkington, S.; Papaefthymiou, G. C; Dalton, H.; Hodgson, K. O.; Lippard, S. J. *J. Am. Chem. Soc.* **1991**, *113*, 9219-9235.

2. Anthony, C. *The Biochemistry of the Methylotrophs*; Academic Press: London, 1982.

3. Higgins, I. J.; Best, D. J.; Hammond, R. C.; Scott, D. *Microbiol. Rev.* **1981**, *45*, 556-590.

4. (a) Dalton, H.; Prior, S. D.; Leak, D. J.; Stanley, S. H. *Microb. Growth on C1 Cmpd., Proc. Int. Symp. 1983*; Am. Soc. Microbiol.: Washington D. C, 1984; pp. 75-82.

5. (a) Colby, J. D.; Stirling, I.; Dalton, H. *Biochem. J.* **1977**, *165*, 395-402. (b) Prior, S. D.; Dalton, H. *J. Gen. Microbiol.* **1985**, *131*, 155-163. (c) Burrows, K. J.; Cornish, A.; Scott, D.; Higgins, I. J. *J. Gen. Microbiol.* **1984**, *130*, 3327-3333.

6. Stanley, S. H.; Prior, S. D.; Leak, D. J.; Dalton, H. *Biotech. Lett.* **1983**, *5*, 487-492.

7. Prior, S. D.; Dalton, H. *J. Gen. Microbiol.* **1985**, *131*, 155-163.

8. (a) Akent'eva, N. P.; Stukan, R. A.; Prusakov, V. E.; Tsuprun, V. L.; Gvozdev, R. I.; Shushenecheva, E. V. *Biocatalysis* **1990**, *4*, 39-53. (b) Akent'eva, N. P.; Gvozdev, R. I. *Biokhimiya* **1988**, *53*, 91-96. (c) Korshunova, L. A.; Akent'eva, N. P.; Gvozdev, R. I.; Shushenacheva, E. V. *Biokhimiya* **1989**, *54*, 1652-1657.

9. Tonge, G. M.; Harrison, D. E. F.; Higgins, I. J. *Biochem. J.*, **1977**, *161*, 333-344.

10. (a) Colby, J.; Dalton, H. *Biochem. J.* **1978**, *171*, 461-468. (b) Patel, R. N. *Microb. Growth on C1 Cmpd., Proc. Int. Symp. 1983*; Am. Soc. Microbiol.: Washington D. C, 1984; pp. 83-90. (c) Fox, B. G.; Lipscomb, J. D. *Biochem. Biophys. Res. Comm.* **1989**, *154*, 165-170.

11. Colby, J.; Dalton, H. *Biochem. J.* **1976**, *157*, 495-497.

12. Stirling, D. I.; Dalton, H. *J. Biochem.*, **1979**, *96*, 205-212.

13. (a) Colby, J.; Stirling, D. I.; Dalton, H. *Biochem. J.* **1977**, *165*, 395-402. (b) Stirling, D. I.; Colby, J.; Dalton, H. *Biochem. J.* **1979**, *177*, 361-364. (c) Leak, D. J.; Dalton, H. *J. Gen. Microbiol.* **1983**, *129*, 3487-3497. (d) Fox, B. G.; Borneman, J. G.; Wackett, L. P.; Lipscomb, J. D. *Biochemistry*, **1990**, *29*, 6419-6427. (e) Hou, C. T.; Patel, R. N.; Laskin, A. I.; Barnabe, N. *FEMS Microbiol. Lett.* **1980**, *9*, 267-270.

14. Ortez de Montellano, P. R., Ed. *Cytochrome P-450: Structure, Mechanism, and*

Biochemistry; Plenum Press: New York, 1986.

15. (a) Jezequel, S. G.; Higgins, I. J. *J. Chem. Tech. Biotechnol.* **1983**, *33B*, 139-144. (b) Green, J.; Dalton, H. *J. Biol. Chem.* **1989**, *264*, 17698-17703. (c) Ruzicka, F.; Huang, D.-S.; Donnelly, M. I.; Frey, P. A. *Biochemistry*, **1990**, *29*, 1696-1700.

16. Green, J.; Dalton, H. *Biochem. J.* **1989**, *259*, 167-172.

17. (a) Murch, B. P.; Bradley, F. C.; Que, L. Jr. *J. Am. Chem. Soc.* **1986**, *108*, 5027-5028. (b) Vincent, J. B.; Huffman, J. C.; Christou, G.; Li, Q.; Nanny, M. A.; Hendrickson, D. N.; Fong, R. H.; Fish, R. H. *J. Am. Chem. Soc.* **1988**, *110*, 6898-6900. (c) Kitajima, N.; Fukui, H.; Moro-oka, Y. *J. Chem. Soc., Chem. Commun.* **1988**, 485.

18. Westrick, L.L.; Mello, J. W.; Thomas, R. F. *J. Am Water Works Assoc.* **1984**, *76*, 52-59.

19. (a) Bouwer, E. J.; McCarty, P. L. *App. Environ. Microbiol.* **1983**, *45*, 1286-1294. (b) Parsons, F.; Wood, P. R.; DeMarco, J. *J. Am Water Works Assoc.* **1984**, *76*, 56-59. (c) Vogel, T. M.; McCarty, P. L. *Appl. Environ. Microbiol.* **1985**, *49*, 1080-1083. (d) Vogel, T. M.; Criddle, C. S.; McCarty, P. L. *Environ. Sci. Technol.* **1987**, *21*, 722-736.

20. Wilson, J. T.; Wilson, B. H. *Appl. Environ. Microbiol.* **1985**, *49*, 242-243.

21. (a) Henry, S. M.; Grbic-Galic, D. *Microb. Ecol.* **1990**, *20*, 151-169. (b) Henry, S. M.; Grbic-Galic, D. *Appl. Environ. Microbiol.* **1991**, *57*, 236-244.

22. Semprini, L.; Robers, P. V.; Hopkins, G. D.; McCarty, P. L. *Groundwater*, **1990**, *28*, 715-727.

23. (a) Colby, J.; Dalton, H. *Biochem. J.* **1979**, *177*, 903-908. (b) Woodland, M. P.; Dalton, H. *Anal. Biochem.* **1984**, *139*, 459-462. (c) Lund, J.; Dalton, H. *Eur. J. Biochem.* **1985**, *147*, 292-296. (d) Patel, R. N.; Savas, J. C. *J. Bacteriol.* **1987**, *169*, 2313-2317.

24. (a) Woodland, M. P.; Patil, D. S.; Cammack, R.; Dalton, H. *Biochim. Biophys. Acta* **1986**, *873*, 237-242. (b) Fox, B. G.; Surerus, K. K.; Münck, E.; Lipscomb, J. D. *J. Biol. Chem.* **263**, 10553-10556.

25. (a) Colby, J.; Dalton, H. *Biochem. J.* **1979**, *177*, 903-908. (b) Lund, J.; Dalton, H. *Eur. J. Biochem.* **1985**, *147*, 292-296. (c) Prince, R. C.; Patel, R. N. *FEBS* **1986**, *203*, 127-130. (d) Patel, R. N. *Arch. Biochem. Biophys.* **1987**, *252*, 229-236.

26. Green, J.; Dalton, H. *J. Biol. Chem.* **1985**, *260*, 15795-15801.

27. (a) Lund, J. ; Woodland, M. P.; Dalton, H. *Eur. J. Biochem.* **1985**, *147*, 297-305. (b) Green, J. ; Dalton, H. *Biochem. J.* **1989**, *259*, 167-172.

28. Orme-Johnson, W. H.; Beinert, H. *J. Biol. Chem.* **1969**, *244*, 6143-6148.

29. (a) Dalton, H. *Adv. Appl. Microbiol.* **1980**, *26*, 71-87. (b) Dalton, H. *Microbial Growth of C1 Compounds*; Heyden Press: London, 1980, pp 1-10.

30. Fox, B. G.; Froland, W. A.; Dege, J. E.; Lipscomb, J. D. *J. Biol. Chem.* **1989**, *264*, 10023-10033.

31. Fox, B. G.; Liu, Y.; Dege, J. E.; Lipscomb, J. D. *J. Biol. Chem.* **1991**, *266*, 540-550.

32. Froland, W. A.; Andersson, K. K.; Lee, S.-K.; Liu, Y.; Lipscomb, J. D. *J. Biol. Chem.* **1992**, *267*, 17588-17597.

33. (a) Lippard, S. J. *Angew. Chem. Int. Ed. Engl.* **1988**, *27*, 344-361. (b) Sanders-Loehr, J. *Iron Carriers and Iron Proteins*; VCH Publishers Inc.: New York, 1989; pp. 373-466. (c) Que, L., Jr.; True, A. E. *Prog. Inorg. Chem.* **1990**, *38*, 97-200.

34. Kurtz, D. M. Jr. *Chem. Rev.* **1990**, *90*, 585-606.

35. The generalizations made for hydroxo-bridged models in the following discussion also hold for alkoxo-bridged models, in which an alkoxide group replaces the hydroxide group. The spectroscopic values reviewed are for diferric model compounds. Models containing porphyrin ligation are not included in this discussion.

36. Reem, R. C.; McCormick, J. M.; Richardson, D. E.; Devlin, F. J.; Stephens, P. J.; Musselman, R. L.; Solomon, E. I. *J. Am. Chem. Soc.* **1989**, *111*, 4688-4704.

37. (a) Sanders-Loehr, J.; Wheeler, W. D.; Shiemke, A. K.; Averill, B. A.; Loehr, T. M. *J. Am. Chem. Soc.* **1989**, *111*, 8084-8093. (b) Sanders-Loehr, J.; Loehr, T. M.; Mauk, A. G.; Gray, H. B. *J. Am. Chem. Soc.* **1980**, *102*, 6992-6996.

38. Gorun, S. M.; Lippard, S. J. *Inorg. Chem.* **1991**, *30*, 1625-1630.

39. (a) Hendrickson, W. A.; Co, M. S.; Smith, J. L.; Hodgson, K. O.; Klippenstein, G. L. *Proc. Natl. Acad. Sci. USA* **1982**, *79*, 6255-6259. (b) Elam, W. T.; Stern, E. A.; McCallum, J. D.; Sanders-Loehr, J. *J. Am. Chem. Soc.* **1982**, *104*, 6369-6373. (c) Elam, W. T.; Stern, E. A.; McCallum, J. D.; Sanders-Loehr, J. *J. Am. Chem. Soc.* **1983**, 1919-1923. (d) Zhang, K.; Stern, E. A.; Ellis, F.; Sanders-Loehr, J.; Shiemke, A. K. *Biochemistry* **1988**, *27*, 7470-7479. (e) Scarrow, R. C.; Maroney, M. J.; Palmer, S. M.; Que, Jr., L.; Roe, A. L.; Salowe, S. P.; Stubbe, J. *J. Am. Chem. Soc.* **1987**, *109*, 7857-7864. (f) Scarrow, R. C.; Maroney, M. J.; Palmer, S. M.; Que, L., Jr.; Roe, A. L.; Salowe, S. P.; Stubbe, J. *J. Am. Chem. Soc.* **1986**, *108*, 6832-6834. (g) Bunker, G.; Petersson, L.; Sjöberg, B.-M.; Sahlin, M.; Chance, M.; Chance, B.; Ehrenberg, A. *Biochemistry* **1987**, *26*, 4708-4716. (h) Kauzlarich, S. M.; Teo, B. K.; Zirino, T.; Burman, S.; Davis, J. C.; Averill, B. A. *Inorg. Chem.* **1986**, *25*, 2781-2785.

(i) True, A. E.; Scarrow, R. C.; Holz, R. C.; Que, L., Jr. *Inorg. Biochem.* **1991**, *43*, 545.

40. (a) Stenkamp, R. E.; Sieker, L. C.; Jensen, L. H. *J. Am. Chem. Soc.* **1984**, *106*, 618-622. (b) Stenkamp, R. E.; Sieker, L. C.; Jensen, L. H.; McCallum, J. D.; Sanders-Loehr, J. *Proc. Natl. Acad. Sci. USA* **1985**, *82*, 713-716. (c) Nordlund, P.; Sjöberg, B.-M.; Eklund, H. *Nature* **1990**, *345*, 593-598.

41. An excellent, detailed discussion of the theory, practice and applications of X-ray absorption spectroscopy appears in *X-ray Absorption: Principles, Applications, Techniques of EXAFS, SEXAFS, and XANES*; Koningsberger, D. C., Prins, R., eds.; John Wiley and Sons Inc.: NewYork, 1988.

42. Cramer, S. P. in *X-ray Absorption: Principles, Applications, Techniques of EXAFS, SEXAFS, and XANES*; Koningsberger, D. C., Prins, R., eds.; John Wiley and Sons Inc.: NewYork, 1988; pp 257-320.

43. Bianconi, A. in *X-ray Absorption: Principles, Applications, Techniques of EXAFS, SEXAFS, and XANES*; Koningsberger, D. C., Prins, R., eds.; John Wiley and Sons Inc.: NewYork, 1988; pp 573-662.

44. Scott, R. A. *Methods Enzymol.* **1985**, *117*, 414-459.

45. Heald, S. M. in *X-ray Absorption: Principles, Applications, Techniques of EXAFS, SEXAFS, and XANES*; Koningsberger, D. C., Prins, R., eds.; John Wiley and Sons Inc.: NewYork, 1988; pp 87-162.

46. Stern, E. A. in *X-ray Absorption: Principles, Applications, Techniques of EXAFS, SEXAFS, and XANES*; Koningsberger, D. C., Prins, R., eds.; John Wiley and Sons Inc.: NewYork, 1988; pp 3-51.

47. Cramer, S. P.; Hodgson, K. O. *Prog. Inorg. Chem.* **1979**, *25*, 1-39.

48. MacGillavry, C. H.; Rieck, G. D., Ed.: *International Tables for X-ray Crystallography Vol. III*, Kynoch Press: Birmingham, England, 1968.

49. Cramer, S. P.; Tench, O.; Yocum, M.; George, G. N. *Nucl. Instrum. Methods Phys. Res.* **1988**, *A266*, 586-591.

50. Teo, B.-K.; Lee, P. A. *J. Am. Chem. Soc.*, **1979**, *101*, 2815-2832.

51. McKale, A. G.; Veal, V. W.; Paulikas, A. P.; Chan, S.-K.; Knapp, G. S. *J. Am. Chem. Soc.* **1988**, *110*, 3763-3768.

52. Teo, B.-K.; Antonio, M. R.; Averill, B. A. *J. Am. Chem. Soc.* **1983**, *105*, 3751-3762.

53. Cramer, S. P.; Hodgson, K. O.; Stiefel, E. I.; Newton, W. E. *J. Am. Chem. Soc.* **1978**, *100*, 2748-2761.

Chapter 2

X-ray Absorption Spectroscopic Studies of the Dinuclear Non-Heme Iron Center in the Hydroxylase Component of Methane Monooxygenase and the B2 subunit of Ribonucleotide Reductase

2.1. Introduction

Methanotrophic bacteria oxidize methane to carbon dioxide for growth and energy.[1] The initial and most difficult step in the reaction is the incorporation of oxygen into methane to yield methanol. This step is catalyzed by methane monooxygenase (MMO), a multi-component enzyme present in both type I and type II methanotrophs. Type I and type II methanotrophs, which differ in their intracytoplasmic membrane structure and their carbon assimilation pathways,[2] express MMO in either a particulate or soluble form depending primarily on the concentrations of copper and oxygen present during bacterial growth.[3] Particulate MMO is a copper-containing membrane-bound protein,[4] while soluble MMO contains a non-heme iron center and is associated with the soluble fractions of cellular extracts.[5] MMO in both the particulate and soluble form is a non-specific enzyme that catalyzes the oxidation of a wide variety of substrates, including aliphatic, aromatic, cyclic and halogenated compounds,[6] a property which makes methanotrophs interesting as a possible biocatalyst.

Soluble MMO from *Methylococcus capsulatus* (Bath),[7] a type I methanotroph, and *Methylosinus trichosporium* OB3b,[5c] a type II methanotroph, has been resolved into three components, which are called the hydroxylase, the reductase, and component B. Soluble MMO from *Methylobacterium* sp. Strain CRL-26, also type II, has been resolved into only two components, identified as the hydroxylase and the reductase.[8] The reductase component[9] (Mr 42,000), formerly protein C, is an iron-sulfur flavoprotein containing one FAD and one Fe_2S_2 cluster. The reductase mediates the transfer of electrons one at a time from NADH to the hydroxylase component[8a,10] (Mr 250,000), via its FAD and Fe_2S_2 redox centers.[11] The third component, component B[12] (Mr 15,700), contains no prosthetic groups or metals and is believed to serve a regulatory role, linking electron transfer from the reductase to the hydroxylase to substrate oxidation. Recent studies of a very high specific activity hydroxylase from *M. trichosporium* OB3b has verified that the hydroxylase is the site of substrate binding and oxygen activation, and that monooxygenase activity is associated with the fully reduced form of the hydroxylase.[10b]

The hydroxylase component (formerly Protein A) is a non-heme protein containing 2-4 irons per unit depending on growth and harvesting conditions. It contains no acid-labile sulfur, and is made up of 3 smaller subunits in an $\alpha_2\beta_2\gamma_2$ polypeptide arrangement. EPR studies[13] of the hydroxylase component of MMO have suggested that the protein belongs to the class of non-heme dinuclear iron proteins which includes hemerythrin (Hr), ribonucleotide reductase (RRB2), purple acid phosphatase (PAP) and uteroferrin (Uf).[14] Structural studies on the dinuclear iron centers in these proteins are critical to understanding

the functional differences between the spectroscopically similar active sites (for a review of the spectroscopic properties, see reference 14b).

Structural studies of the non-heme dinuclear iron center in the hydroxylase component of MMO along with relevant model compounds using extended X-ray absorption fine structure (EXAFS) have been initiated.[15] EXAFS has proven to be very sensitive to the presence or absence of μ-oxo bridges in dinuclear iron proteins and model compounds.[16] Most notably, the EXAFS modulations of μ-oxo bridged diferric models are remarkably similar to each other and different from the EXAFS of μ-hydroxo bridged diferric models. Also, the short Fe-O distance of the $[Fe_2O]^{+4}$ core in model compounds and proteins is distinctly resolved from the longer first shell N/O ligands in the fits to the EXAFS data and a short Fe-O contribution (at ~ 1.8 Å) is required to obtain an adequate fit to the data.[16]

Previous EXAFS experiments have been done on the oxidized and reduced forms of the hydroxylase of MMO from *M. capsulatus* (Bath)[15] and on the oxidized form of the hydroxylase from *M. trichosporium* OB3b.[15b] The oxidized protein samples from these experiments were photoreduced by the X-ray beam to the semimet state. Analysis of the EXAFS data on the semimet protein suggested that the protein does not contain a μ-oxo bridge in its dinuclear iron center. An EXAFS study on the oxidized hydroxylase of MMO from *Methylobacterium* sp. Strain CRL-26 did not conclusively determine the presence or absence of a μ-oxo or μ-hydroxo bridge due to the limited *k*-range of the EXAFS data, although the iron-iron distance determined (3.05 Å) is in the range of those found for some μ-oxo bridged models and proteins as well as some dibridged models.[17]

Fe K-edge EXAFS data has been collected on samples of the hydroxylase of MMO from *Methylococcus capsulatus* (Bath) in its oxidized and reduced forms to add to the information obtained in the previous studies on the photoreduced semimet forms of the hydroxylase. EXAFS data on a diferric form of the protein was collected, with no photoreduction of the protein to its semimet state. In addition, EXAFS data on the reduced form of the iron center in the B2 subunit of ribonucleotide reductase has been collected. The results of the experiments on the hydroxylase samples, including details about protein purification and characterization by Mössbauer and EPR spectroscopy have been reported elsewhere.[18] Details of the analysis of the Fe K-edge EXAFS of these samples and the earlier samples, as well as the results of the analysis for the ribonucleotide reductase data will be presented here.

2.2. Experimental

2.2.1. EXAFS Sample Preparation

Soluble hydroxylase from *Methylococcus capsulatus* (Bath) and *Methylosinus trichosporium* (OB3b) were obtained as discussed before. Purified hydroxylase was diluted in buffer and frozen at -80° C until further use. The hydroxlase was then thawed and concentrated to approximately 11 mg protein /ml using an Amicon PM 10 membrane. The hydroxylase complexes were dialyzed into a 50% ethylene glycol solution of an appropriate buffer[18] and further concentrated on a Centricon centrifugal microconcentrator. The samples were then degassed and brought into a wet box. Samples **EXAFS2**, **EXAFS4**, and **EXAFS5** were loaded into lucite EXAFS cells (23 mm x 2 mm x 3mm, ~ 140 µl volume) with 25 µm Kapton windows. **EXAFS3** and **EXAFS6** were reduced to the diferrous state by incubating the samples for 25 minutes with a 10-fold molar excess of dithionite in the presence of 100 µM methyl viologen and 10 µM proflavin, and then loaded into the lucite EXAFS cells. The samples were immediately frozen in liquid nitrogen upon removal from the wet box and stored in a LN_2 refrigerator. **EXAFS1** was prepared as previously described.[15a] The sample of ribonucleotide reductase was reduced in the same manner as described above for the hydroxylase samples.

2.2.2. Data Collection, Reduction and Analysis

A summary of the samples is presented in Table 2.1. All protein sample data were measured in fluorescence mode at 10 K maintained by using an Oxford Instruments continuous flow liquid helium CF1208 cryostat. The **EXAFS1** sample was run at SSRL on focused beamline 2-2 during dedicated conditions (3 GeV, 50-65 mA) by using a Si(111) double-crystal monochromator tuned 100% at 7850 eV.[19] The fluorescence signal was detected with an Ar-filled ionization chamber,[20] equipped with Soller slits and a Mn filter. **EXAFS2**, **EXAFS3**, and **EXAFS4** samples were run at SSRL on focused wiggler beamline 4-2 during dedicated conditions by using a Si(111) double-crystal monochromator tuned 100% at 7968 eV, and the same detector setup as for **EXAFS1**. **EXAFS5** sample was run at NSLS on unfocused beamline X-19A (2.5 GeV, 90-200 mA) by using a Si(220) double-crystal monochromator detuned for harmonic rejection to 66% of the maximum at 7375 eV. The fluorescence signal was monitored by using a 13-element Ge solid state array detector[21] windowed on the Fe Kα signal. During the experiment, count rates of approximately 37,000/s (total per element) were measured at

Table 2.1. Sample and Data Collection Summary.

Sample	Description	Data Collection Information[a]	[Fe] mM	Scans avg/scans collected
EXAFS1[b]	*M. capsulatus* Oxidized ⟶ semimet	Jan. 1987; SSRL 2-2; Si(111); 10K; focused	4.0	22/32
EXAFS2[b]	*M. capsulatus* Oxidized ⟶ semimet	Nov. 1987; SSRL 4-2; Si(111); 10K; focused	4.0	22/32
EXAFS3	*M. capsulatus* Reduced	Nov. 1987; SSRL 4-2; Si(111); 10K; focused	4.0	24/29
EXAFS4[b]	*M. trichosporium* Oxidized⟶ semimet	Nov. 1987; SSRL 4-2; Si(111); 10K; focused	4.0	6/13
EXAFS5	*M. capsulatus* Oxidized	June 1989; NSLS X19A; Si (220); Sept. 1989; NSLS X19A; Si(111); 10K; unfocused	4.0	199/235 (19)[c]
EXAFS6	*M. capsulatus* Reduced	Sept. 1989; NSLS X19A; Si(111); 10K; unfocused	4.0	228/260 (20)[c]
RRB2	*E. coli* Reduced	June 1992; SSRL 7-3; Si(220); 10K; unfocused	2.0	308/377 (29)[c]

[a]SSRL - Stanford Synchrotron Radiation Laboratory. NSLS - National Synchrotron Light Source. Unless otherwise noted, an ionization chamber of the Stern/Lytle design[20] was used to detect the fluorescence. [b]Sample was photoreduced to the semimet state by the X-ray beam. Only the scans after photoreduction was complete were averaged for further analysis. [c]A 13-element Ge solid state array detector was used to detect the fluorescence. 13 channels of data were collected for each scan. The numbers represent the total number of channels averaged/total channels collected. The number in parentheses is the number of scans collected (for **EXAFS5**, only 12 channels were working for 12 of the 19 scans collected).

7375 eV. The **EXAFS5** sample was again measured at NSLS on beamline X-19A along with **EXAFS6** under the same conditions as the first **EXAFS5** experiment, except that a Si(111) double-crystal monochromator detuned to 50% of the maximum at 7820 eV was employed. Count rates of approximately 28,000/s (total per element) at 7800 eV were measured for the Ge detector during this experiment. The **RRB2** data was measured at SSRL on beamline 7-3 using a Si(220) double-crystal monochromator detuned 45% at 7997 eV at 10 K using the Ge fluorescence detector.

Data reduction was performed according to methods described in detail elsewhere[22] but briefly summarized here. Energies were calibrated by using an internal iron foil standard,[23] assigning the first inflection point of the Fe absorption edge as 7111.2 eV. Calibrated scans were inspected individually and rejected if the signal-to-noise level was too high compared to the other scans as a result of beam instabilities or poor detector statistics, or because a beam loss occurred during the scan. In the case of the photoreduced samples **EXAFS1**, **EXAFS2** and **EXAFS4**, the edge shifted during the first approximately four hours of irradiation. These scans were excluded from the subsequent weighted average of scans used in the data analysis.

The same oxidized protein sample (**EXAFS5**) was run twice with different monochromators (Table 2.1), giving rise to different background functions and glitch effects. An average of each data set was done separately (108/144 "scans" for the June 1989 data and 91/91 "scans" for the September 1989 data), the two averages were normalized to each other, and the EXAFS of the two files were averaged before fits were performed on the merged data. Monochromator glitches were edited out of the **EXAFS5** individual averages, as well as the **EXAFS3** and **EXAFS6** average files using a single point replacement method (2, 4 and 2 points total edited, respectively).

A pre-edge subtraction was performed by fitting the EXAFS region with a smooth polynomial which was extrapolated into the pre-edge region and subtracted. A three-segment spline was fit to the EXAFS region and subtracted and the data normalized to an edge jump of one. The spline was chosen so that it minimized residual low frequency background but did not reduce the EXAFS amplitude as checked by monitoring the Fourier transform of the EXAFS during the background subtraction process. The normalized, background-subtracted data were converted to k space, where k is the photoelectron wavevector defined by $[2m_e(E - E_o)/\hbar^2]^{1/2}$. In this expression, m_e is the electron mass, E is the photon energy, $\hbar$ is Planck's constant divided by 2π, and E_o is the threshold energy, 7130 eV (where k is defined to be zero).

Analysis was performed with non-linear least squares curve fitting techniques[22,23] using empirical phase and amplitude parameters, as described previously.[22] The following

models were used to obtain the empirical Fe-X backscattering parameters of interest: Fe-O and Fe-C from [Fe(acetylacetonate)$_3$];[24] Fe-N from [Fe(1,10-phenanthroline)$_3$](ClO$_4$)$_3$;[25] Fe-Fe from the tribridged models [Fe$_2$(OH)(OAc)$_2$(HB(pz)$_3$)$_2$](ClO$_4$)[26a] (**FEHBPZOH**) and [Fe$_2$O(OAc)$_2$(HB(pz)$_3$)$_2$][28b] (**FEHBPZO**). Data for these model compounds were collected as described previously.[15a]

For all the data presented, Fourier transforms (from k to R space) of 3.5 - 12.5 Å^{-1} and 3.5 - 10.8 Å^{-1} were performed and two data ranges, from 4.0 - 12.0 Å^{-1} and 3.8 - 10.0 Å^{-1}, respectively, were fit. A gaussian window of 0.1 Å was used for all transforms. The window widths used in the backtransforms (from R to k space) are listed in the tables. They were kept as similar as possible to each other, as well as to the windows used to extract amplitude and phase parameters from the models, to minimize artifacts introduced by the Fourier filtering technique. All curve fitting was based on k^3-weighted data and applied to individual filtered shells as well as to wide-range filtered shells and to the raw data. Only the structure-dependent parameters, i.e. the distance and the number of atoms in the shell, were varied except where otherwise noted. For example, in the first shell fits the same Debye-Waller factor as determined for the models was used in fitting the proteins and the coordination number was varied. A "goodness-of-fit" parameter, F, was calculated as $F = \{[k^6(\text{data} - \text{fit})^2]/(\text{no. of points})\}^{1/2}$ for each fit.

2.3. Results of XAS Experiments

The k^3-weighted EXAFS of the protein samples **EXAFS2-EXAFS6** are presented in Figure 2.1 and the Fourier transforms in Figure 2.2 (for **EXAFS1**, see reference 15a). The oxidized protein EXAFS are compared to the EXAFS of the model compounds **FEHBPZOH** and **FEHBPZO** in Figure 2.3, and shows strong similarity to the **FEHBPZOH** EXAFS. This suggests that the structure of the active site of the protein resembles the iron center of the hydroxo-bridged model compound. The EXAFS of the semimet protein samples (Figure 2.1b,c) have maxima (at ~ 7 and 11 Å^{-1}) that are only shoulders in the oxidized protein sample EXAFS. The overall features of the EXAFS of the semimet protein samples from the two bacterial species are similar, despite the higher noise-level for the *M. trichosporium* OB3b sample (**EXAFS4**), as are the Fourier transforms (Figure 2.2b,c) indicating that the active sites of the hydroxylase from the two species are similar. The reduced protein EXAFS maximum around k = 6 Å^{-1} (Figure 2.1d,e) is shifted to lower k relative to the semimet and oxidized protein EXAFS and the first shell peak in the Fourier transform is shifted to higher R (Figure 2.2d,e) suggesting that the first shell coordination around Fe is at a longer distance in the reduced form of the

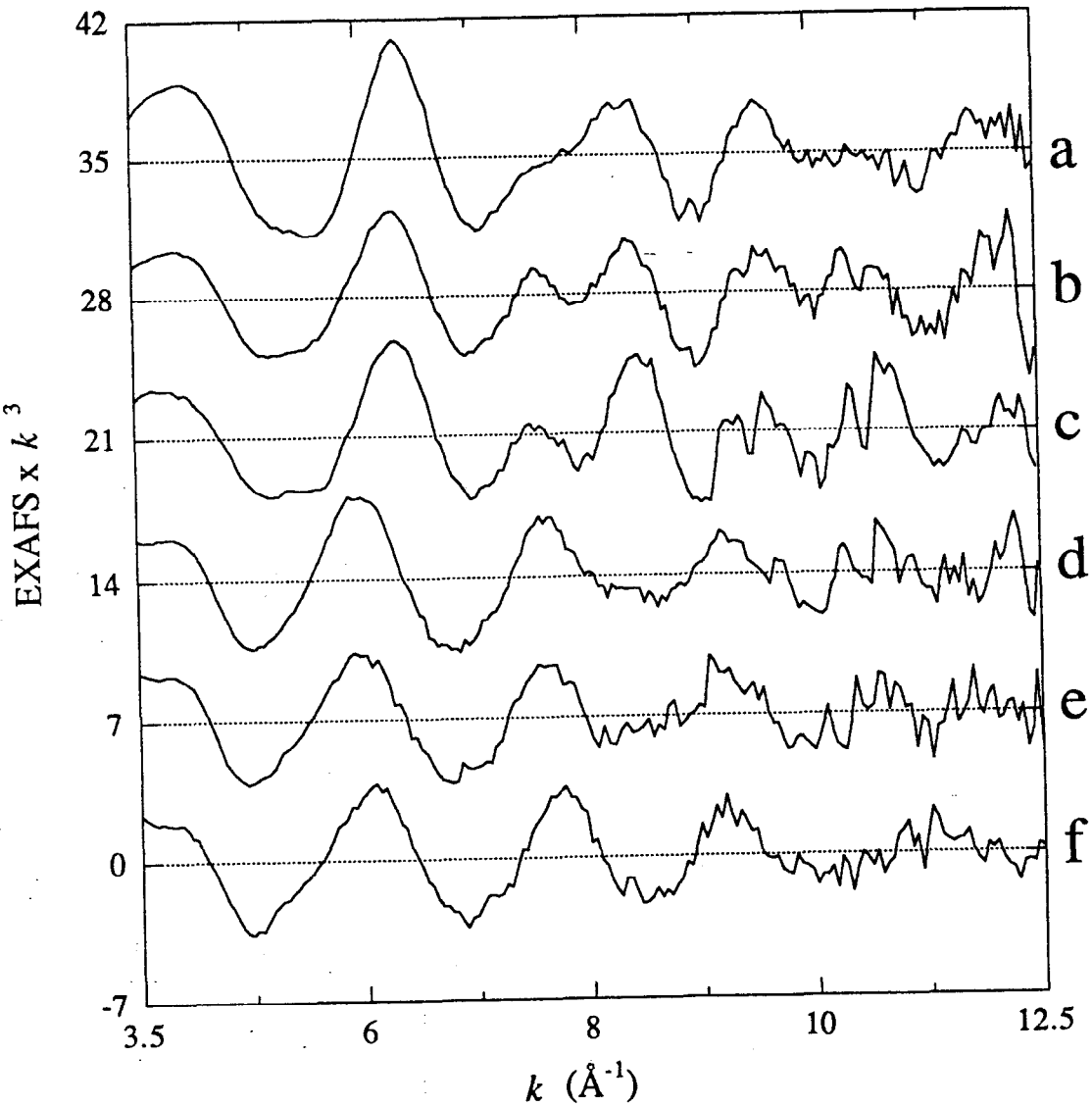

Figure 2.1. EXAFS data of the hydroxylase of MMO: (a) **EXAFS5**, (b) **EXAFS2**, (c) **EXAFS4**, (d) **EXAFS3**, (e) **EXAFS6**; and the B2 subunit of RR: (f) **RRB2**. Note the simpler metrical details of the reduced forms (d-f) over the oxidized and semimet forms. The data shown are the data used for Fourier transforms.

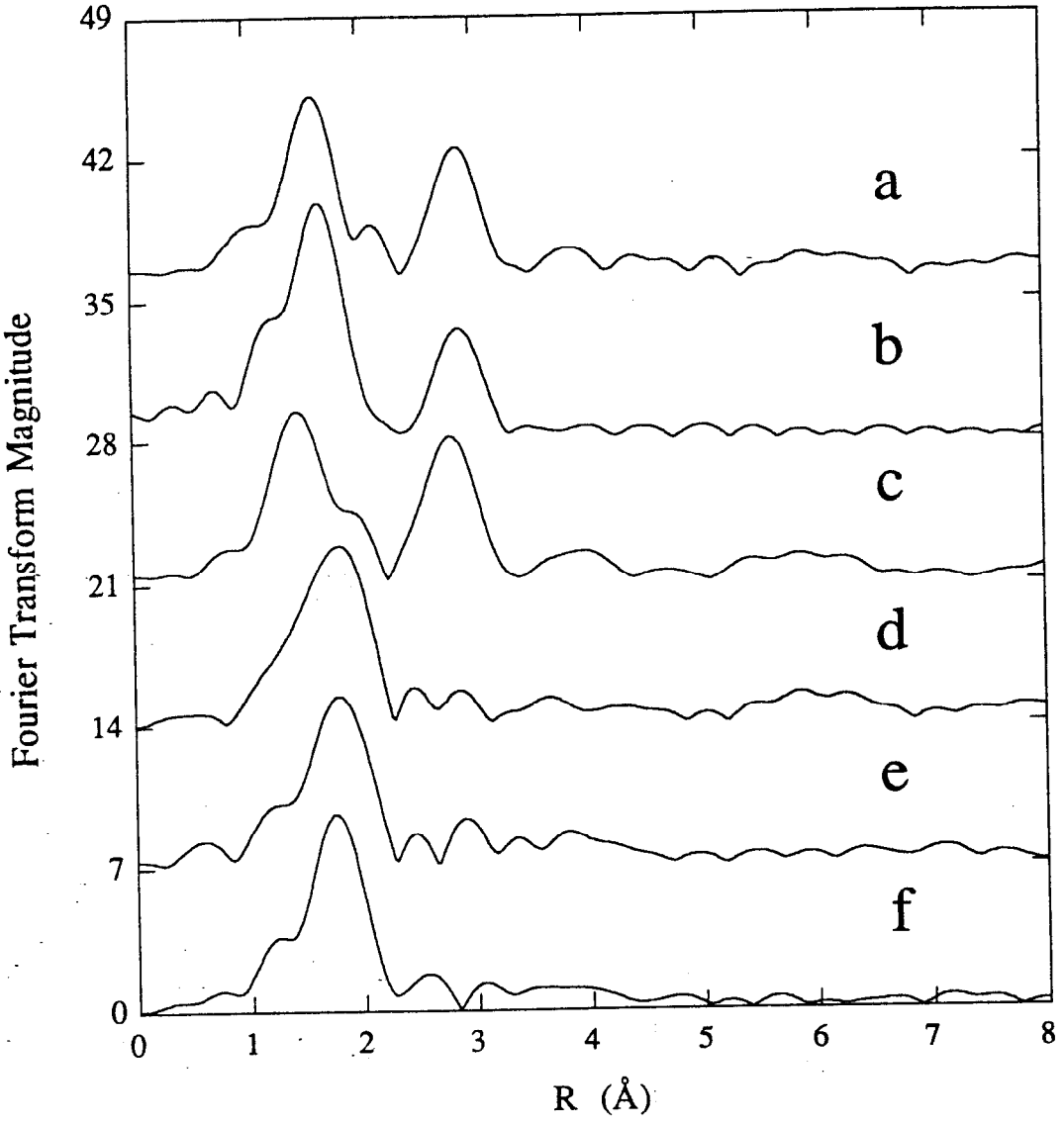

Figure 2.2. Fourier transforms of the EXAFS data presented in Figure 2.1. (a) **EXAFS5**, (b) **EXAFS2**, (c) **EXAFS4**, (d) **EXAFS3**, (e) **EXAFS6**, (f) **RRB2**. Note the absence of the second shell peak in the reduced sample data (d-f)

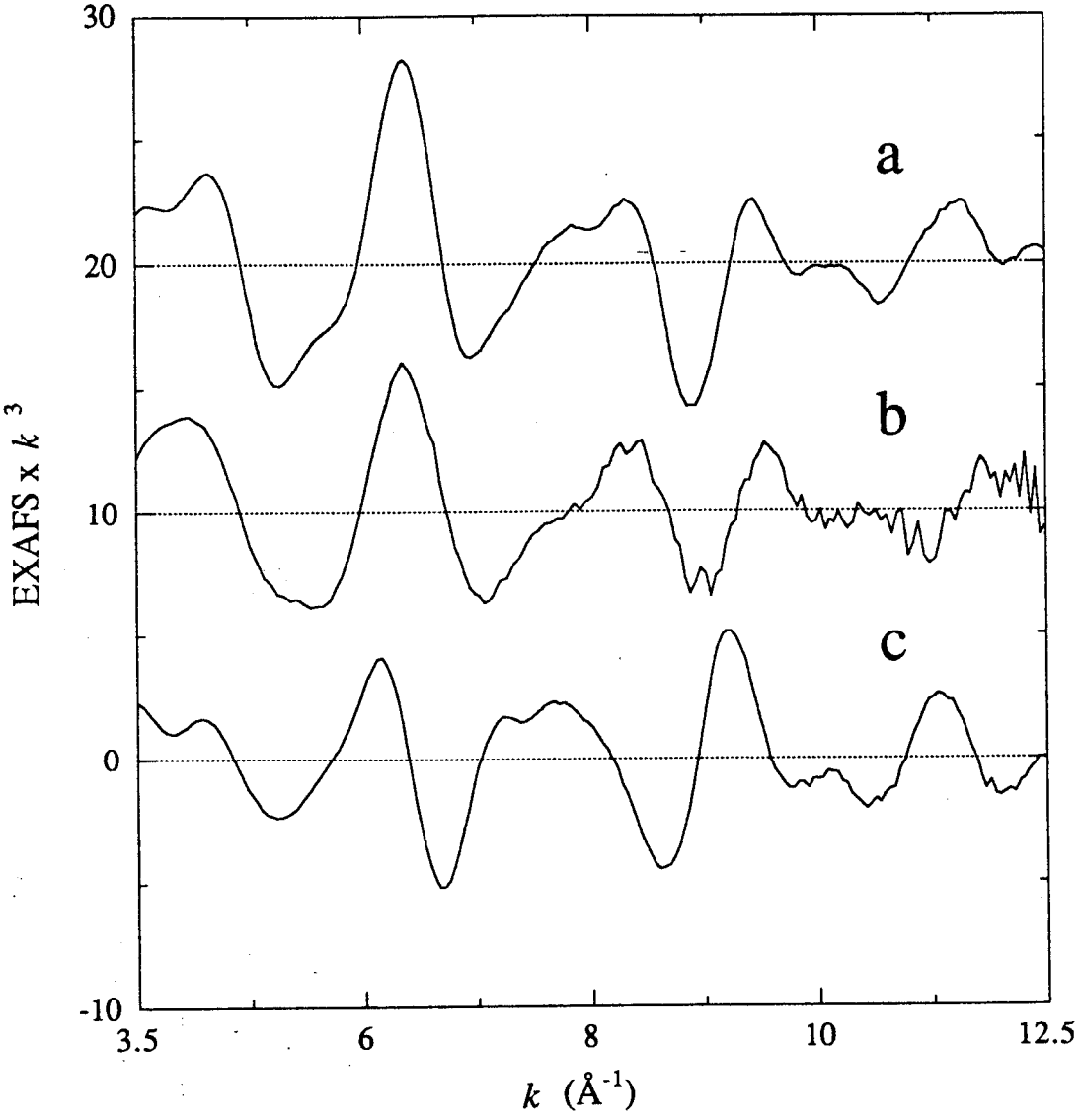

Figure 2.3. A comparison of the EXAFS data for the oxidized hydroxylase data and model compounds: (a) hydroxo-bridged **FEHBPZOH**, (b) **EXAFS5**, (c) oxo-bridged **FEHBPZO**. Note the similarity of the hydroxo-bridged model and hydroxylase EXAFS.

hydroxylase relative to the semimet and oxidized forms. Only one peak is seen in the Fourier transform of the reduced protein EXAFS; the peak attributed to Fe-Fe backscattering is absent, and the overall structure of the reduced protein EXAFS is less complicated than that of the semimet and oxidized protein EXAFS.

2.3.1. Photoreduction of the Oxidized Hydroxylase

The edge position of the first three oxidized protein A samples (**EXAFS1**, **EXAFS2**, and **EXAFS4**) shifted approximately 1.5 eV to lower energy during the first four hours of exposure to the X-ray beam. This shift in energy is due to a 1 e^- photoreduction of the samples to the semimet state by the beam. For the same sample runs, the Fe foil calibrations insured that these shifts were well outside any experimental error. EPR studies on the photoreduced protein samples have verified that the dinuclear iron center was intact after the XAS experiment, giving rise to a typical Fe_2(II,III) spectrum with g values of 1.92, 1.85, and 1.72.[18] In Figure 2.4, the high resolution edge spectra of the non-photoreduced oxidized protein sample (**EXAFS5**), a reduced protein sample (**EXAFS6**, see Chapter 3), and a photoreduced protein sample (**EXAFS7**, see Chapter 3) are presented. Photoreduction of the oxidized protein sample did not occur, due either to the lower incident flux at NSLS compared to SSRL (unfocused bending magnet vs. focused wiggler beamlines) or because the new purification procedure[18] used for this particular sample removed impurities that somehow mediated the photoreduction.

2.3.2. Results of Fits to the Hydroxylase EXAFS Data

2.3.2.1. First Shell Fits. The results of fits to the Fourier filtered first shell data are presented in Table 2.2. The widths of the windows used to isolate the first shell data are listed in Table 2.2. A single N or O contribution could not adequately fit the data, indicating that the first shell contains backscattering atoms at more than one distance and possibly of more than one type. The data could be fit with two contributions, however more than one minima was found, depending on the initial relative Fe-N (R_N) and Fe-O (R_O) bond lengths. EXAFS can not normally discriminate between backscatterers of similar strength as is the case with N and O (which differ only by one in atomic number), giving rise to the multiple minima obtained from the fits. The N and O parameters were correlated over the range of data available, so the fit results reported will correspond to coordination-weighted average distances. The accuracy of this approach has been confirmed in fits to a number of dinuclear non-heme iron models (see Chapter 4).

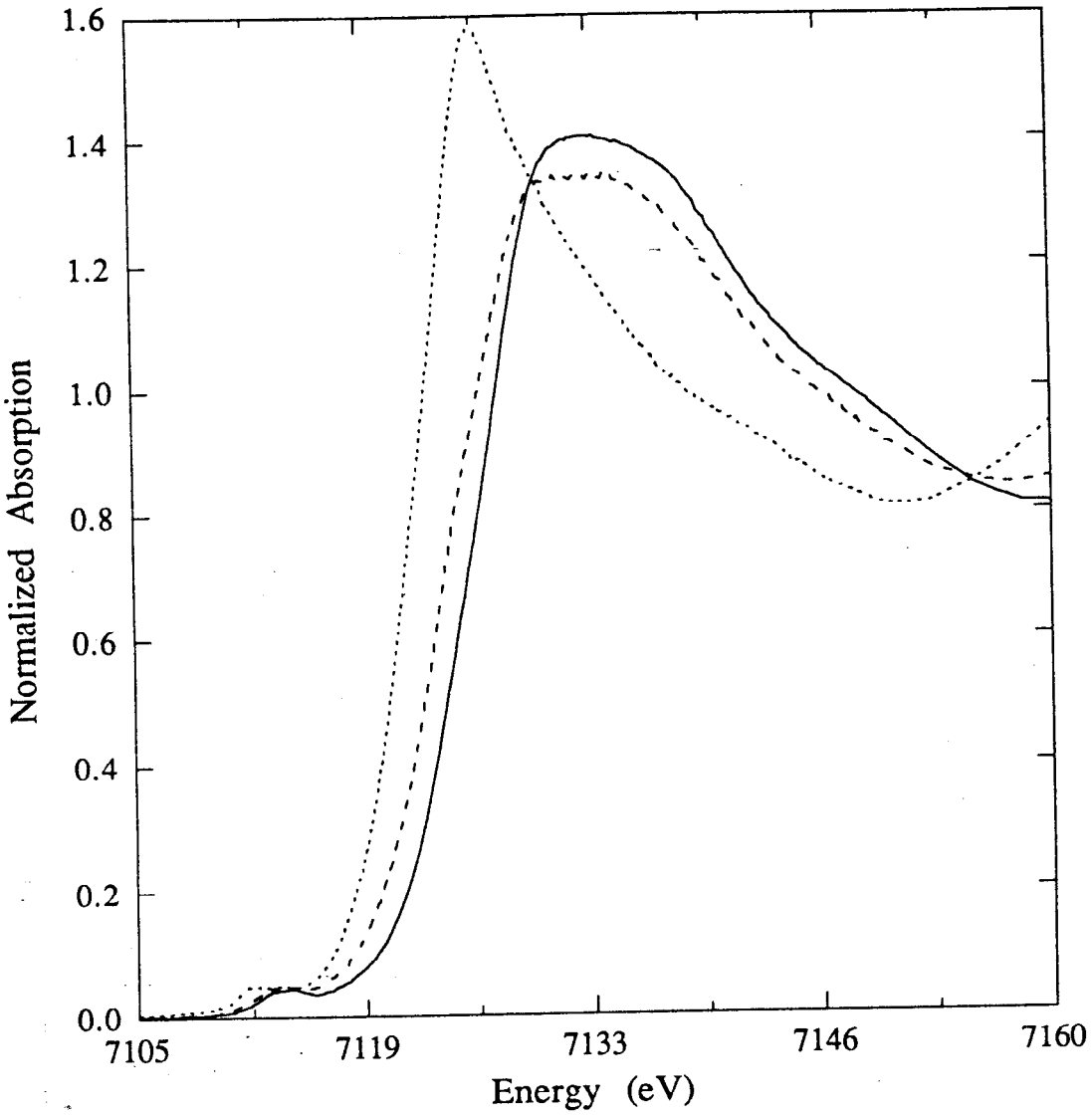

Figure 2.4. The edge positions of the diferric (**EXAFS5**, solid), photoreduced semimet (**EXAFS7**, dash) and diferrous (**EXAFS6**, dot) forms of the hydroxylase of MMO from *M. capsulatus* (Bath).

Table 2.2. Results of First Shell Fits[a] to the Hydroxylase Data.[b]

Sample	Window Width (Å)	Fit	N		O		F
			CN[c]	R(Å)	CN	R(Å)	
EXAFS5	0.75- 2.25	5A	3.4	2.02			1.0
M. capsulatus - ox		5B			3.0	1.99	0.73
		5C	2.3	2.14	3.5	1.97	0.35
		5D	2.7	1.95	3.0	2.06	0.41
EXAFS1	0.70- 1.95	1A	3.0	2.03			0.70
M. capsulatus - sm		1B			2.5	2.00	0.61
		1C	1.6	2.22	3.2	2.00	0.37
		1D	3.7	2.01	1.5	2.14	0.37
EXAFS2	0.70- 2.30	2A	2.3	2.03			0.97
M. capsulatus - sm		2B			2.0	2.01	0.83
		2C	2.5	2.20	3.1	1.99	0.25
		2D	3.4	1.99	2.4	2.13	0.23
EXAFS4	0.70 - 2.15	4A	1.7	2.02			1.2
M. trichosporium -sm		4B			1.6	2.00	1.1
		4C	3.0	2.16	2.8	1.96	0.55
		4D	3.0	1.96	2.8	2.09	0.48

Table 2.2. continued

Sample	Window Width (Å)	Fit	N		O		F
			CN[c]	R(Å)	CN	R(Å)	
EXAFS3	0.60- 2.20	3A	3.2	2.14			0.87
M. capsulatus - red		3B			2.7	2.12	0.63
		3C	2.6	2.24	3.0	2.07	0.30
		3D	2.2	2.05	3.2	2.16	0.29
EXAFS6	0.70- 2.20	6A	2.9	2.15			0.71
M. capsulatus - red		6B			2.5	2.12	0.50
		6C	1.9	2.25	2.7	2.09	0.26
		6D	1.9	2.07	2.6	2.17	0.27
RRB2	0.75 - 2.20	RR-A	3.2	2.12			0.63
Ribonucleotide		RR-B			2.7	2.10	0.42
Reductase B2		RR-C	1.2	2.26	3.1	2.08	0.26
red		RR-D	2.5	2.07	2.1	2.16	0.26

[a]Fitting range $k = 4 - 12$ Å^{-1}. Errors are estimated to be about ± 0.03 Å for distances and 25% for coordination numbers.[22,23] [b]ox = oxidized; sm = semimet; red = reduced. [c]CN = coordination number.

The average of the $R_N > R_O$ minima will be reported because Fe-N distances are generally longer than the Fe-O distances in the model compounds of the dinuclear non-heme center. The coordination-weighted average first shell coordination for the $R_N < R_O$ minima was similar to the average of the other minima, with slightly lower total coordination number and average distance. For the oxidized hydroxylase sample (**EXAFS5**), an average first shell coordination of 5.8 N/O at 2.04 Å was found (Table 2.2, fit 5C). Upon photoreduction to the semimet state, the first shell coordination distance increased to 4.8 N/O at 2.07 Å for **EXAFS1** (Table 2.2, fit 1C), to 5.6 N/O at 2.08 Å for **EXAFS2** (Table 2.2, fit 2C), and to 5.8 N/O at 2.06 Å for **EXAFS4** (Table 2.2, fit 4C). The quality of the fits to the *M. trichosporium* OB3b data set is worse because of the higher noise-level in the data compared to that of *M. capsulatus* (Bath) (only 6 scans were averaged for the *M. trichosporium* OB3b). The average first shell coordination of the reduced protein samples (**EXAFS3** and **EXAFS6**) was found to be 5.1 N/O at 2.15 Å (Table 2.2, fits 3C and 6C). Although the average distance determined is the same for both reduced protein samples, the average coordination number for **EXAFS3** was more than 5 N/O while that for **EXAFS6** was less than 5 N/O, with the difference accounted for primarily in the coordination number of nitrogen.

Fits were also performed on all the protein samples to probe the presence of a short (~ 1.80 Å) Fe-O distance, indicative of an oxo bridged center. When a short Fe-O distance was included, either negative coordination numbers resulted, or the total oxygen contribution was split between two oxygen waves at distances on the order of 2.0 Å. Given the previously shown high sensitivity of EXAFS to the presence or absence of the short oxo bridge,[16] this result, together with the similarity of the oxidized hydroxylase EXAFS spectra to that of **FEHBPZOH** and the dissimilarity to that of **FEHBPZO** (Figure 2.3), clearly indicates that the hydroxylase of methane monooxygenase does not have an oxo bridge in its dinuclear iron center.

2.3.2.2. Second Shell Fits. The **FEHBPZOH** model was chosen as a model for the Fe-Fe interaction in MMO for two reasons: first, in this model the distribution of atoms in the second shell is such that the iron is more isolated from second shell carbon and nitrogen than in the analogous oxo-bridged model, **FEHBPZO** (the nearest C/N shell is 0.26 Å in **FEHBPZOH** and 0.05 Å in **FEHBPZO**[16]); second, since the first shell fits indicate that there is not a μ-oxo bridge in the iron center, a non-μ-oxo bridged model should provide more reliable parameters to use in fits of the protein active site.

Using the empirical amplitude and phase parameters obtained from the **FEHBPZOH** model to fit the second shell hydroxylase data, two Fe-Fe minima were

found, one at ~ 3.0 Å and one at ~ 3.4 Å, depending on the initial Fe-Fe distance used in the fit (Table 2.3). In a subsequent series of Fe-only fits, stepping the initial Fe-Fe distance value in intervals of 0.1 or 0.2 Å from 2.6 to 4.2 Å, it was found that the calculated iron wave moved into phase with the maximum of the amplitude envelope of the second shell data roughly every 0.4 Å, with the best fit (minimum in F and best similarity in shape) and maximum coordination number occurring at the 3.4 Å Fe-Fe distance for **EXAFS1**, **EXAFS2** and **EXAFS5**. The same series of fits was performed by fixing the coordination number at 1 and varying the distance and the Debye-Waller factor, and a minimum in both F and the Debye-Waller factor was found at 3.4 Å (Table 2.4, Figure 2.5) for **EXAFS1**, **EXAFS2** and **EXAFS5**. For the noisier **EXAFS4** data the results were ambiguous, with the fits giving nearly equal preference to the 3.4 and 3.0 Å distances (see comment on shorter data range fits below). As shown in Table 2.3, the two minima obtained for Fe-only fits for **EXAFS1**, **EXAFS2**, **EXAFS4**, and **EXAFS5** were essentially identical, 3.41 - 3.42 Å and 3.03 - 3.04 Å (Table 2.3, fits 1E-F, 2E-F, 4E-4F, and 5E-F). The longer Fe-Fe distance gave a better fit with a larger coordination number and lower F value than the shorter Fe-Fe distance, however the metrical details of the data were not fully explained by the iron contribution, suggesting that something in additon to iron needed to be added to the fits.

The addition of a carbon contribution to the second shell fits, while improving the quality of the fits, confused the details of the fits. The iron and carbon shells were strongly correlated, affecting both the Fe coordination number and distance. The results were once more quite similar for **EXAFS1**, **EXAFS2** and **EXAFS5**, but the Fe-Fe distance was shortened to 3.35 - 3.38 Å and the Fe coordination dropped by a factor of 2 or more when a short (~ 3.0 Å) Fe-C contribution was included (Table 2.3, fits 1J, 2J, and 5J). Attempts to fit the data with the 3.4 Å Fe-distance and a longer Fe-C distance resulted in a second, less well-defined fit with an Fe-C distance of ~ 3.3 Å, and increased Fe-Fe distances of 3.45 - 3.47 Å and coordination numbers (Table 2.3, fits 1I, 2I, and 5I). Fits with a short Fe-Fe distance and a short Fe-C distance resulted in chemically unreasonably short Fe-Fe distances and a decrease in the Fe coordination number (Table 2.3, fits 1K, 2K, and 5K). For **EXAFS4** the 3.4 Å Fe contribution was essentially overshadowed by the 3.04 Å Fe-C wave, and showed very high correlation of the coordination numbers for the fit consisting of the long Fe/long C distances (Table 2.3, fit 4I). The best fit occurred at a very short Fe-Fe distance with the 3.04 Å Fe-C distance (Table 2.3, fit 4J). C-only fits to the data revealed two Fe-C fit minima at ~ 3.0 and 3.4 Å (Table 2.3, fits 1G-H, 2G-H, 4G-H, and 5G-H), with a strong preference for the minimum corresponding to the 3.0 Å

Table 2.3. Results of Second Shell Fits[a] to the Hydroxylase Data.[b]

Sample	Window Width (Å)	Fit	Fe		C		F
			CN[c]	R(Å)	CN	R (Å)	
EXAFS5	2.15- 3.20	5E	1.1	3.42			0.40
M. capsulatus - ox		5F	0.7	3.04			0.65
		5G			5.3	3.05	0.31
		5H			3.8	3.39	0.78
		5I	1.4	3.45	3.9	3.32	0.33
		5J	0.5	3.38	4.0	3.07	0.22
		5K	0.3	2.96	5.4	3.06	0.23
EXAFS1	2.30- 3.40	1E	1.0	3.43			0.46
M. capsulatus - sm		1F	0.6	3.05			0.65
		1G			4.8	3.07	0.41
		1H			3.9	3.40	0.71
		1I	1.2	3.47	4.6	3.34	0.36
		1J	0.6	3.38	4.1	3.10	0.30
		1K	0.3	2.97	5.0	3.08	0.35

Table 2.3. continued

Sample	Window Width (Å)	Fit	Fe		C		F
			CN[c]	R(Å)	CN	R (Å)	
EXAFS2	2.20- 3.40	2E	1.1	3.41			0.61
M. capsulatus - sm		2F	0.8	3.04			0.73
		2G			6.0	3.05	0.38
		2H			4.7	3.39	0.85
		2I	1.6	3.47	7.4	3.33	0.44
		2J	0.5	3.35	5.7	3.07	0.31
		2K	0.02	2.98	5.8	3.06	0.35
EXAFS4	2.10- 3.30	4E	1.3	3.41			0.72
M. trichosporium - sm		4F	1.1	3.04			0.71
		4G			7.3	3.04	0.34
		4H			4.8	3.38	1.09
		4I	2.4	3.46	10.1	3.31	0.41
		4J	0.1	3.37	7.0	3.04	0.34
		4K	0.4	3.02	6.0	3.04	0.25

[a]Fitting range $k = 4 - 12$ Å^{-1}. Errors are estimated to be about ± 0.03 Å for distances and 25% for coordination numbers.[22,23] [b]ox = oxidized; sm = semimet. [c]CN = coordination number.

Table 2.4. Iron Fits to Second Shell Data for Oxidized and Semimet Hydroxylase Samples.[a]

EXAFS5			EXAFS2			EXAFS4		
Fe-Fe (Å)	DW[b]	F	Fe-Fe (Å)	DW	F	Fe-Fe (Å)	DW	F
3.03	0.08240	0.67	3.04	0.07891	0.75	3.04	0.07452	0.68
3.42	0.07578	0.40	3.41	0.07404	0.59	3.40	0.07229	0.70
3.84	0.09105	0.88	3.83	0.09141	1.03	3.82	0.08795	1.20

[a]For these fits, the coordination number was set to 1 and the Fe-Fe distance and Debye-Waller factor were varied. [b]DW = Debye-Waller factor. Initial value = 0.07743.

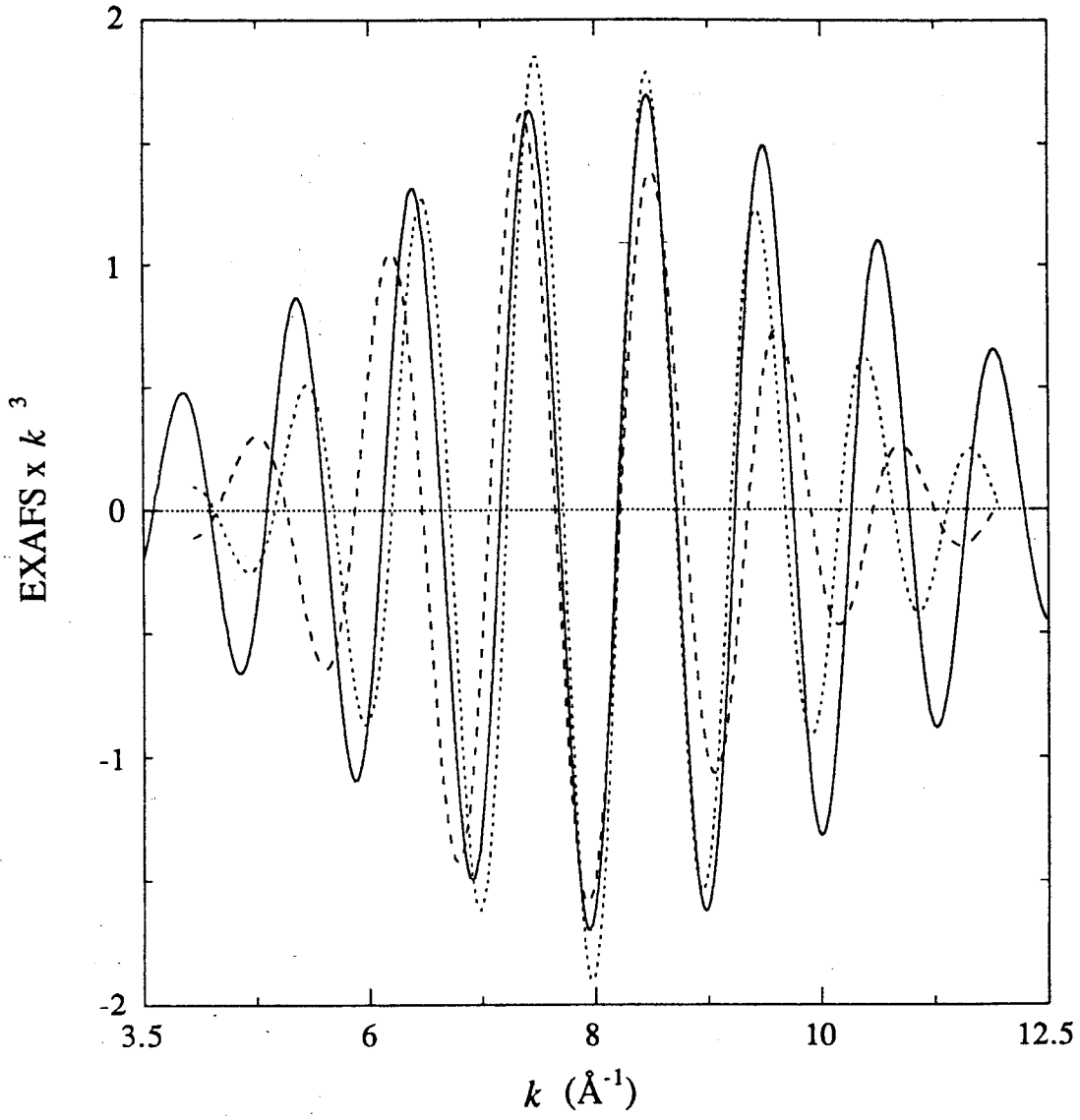

Figure 2.5. Fits to second shell data of **EXAFS5** with iron. The fits were done by fixing the coordination number at 1 and varying the distance and Debye-Waller factor (see Table 2.4). Second shell data (solid), 3.42 Å fit (dot), 3.03 Å fit (dash).

distance. This 3.0 Å Fe-C minimum had a lower F value and was a somewhat better fit to the data than the Fe-only fits for all samples.

For the reduced samples **EXAFS3** and **EXAFS6**, the Fourier transform shows very low intensity in the second shell region compared to the oxidized and semimet hydroxylase Fourier transforms (Figure 2.2d,e). Fits to the reduced hydroxylase data were attempted for a variety of backtransforms. No Fe-only, C-only or Fe + C wave could successfully fit the data.

2.3.2.3. Wide Shell Fits. The same trends and distance information were obtained from fits to EXAFS spectra from wide backtransforms of the data for the oxidized and semimet protein samples (Table 2.5). Addition of Fe to the N and O contribution to the fits was necessary to explain the metrical details of the data and improved the fit dramatically (data for **EXAFS5**, Figure 2.6a,b). The fit function dropped from a value of 1 for **EXAFS5** (Table 2.5, fit 5L) to 0.52 (Table 2.5, fit 5M). The fits which included the short 3.0 Å Fe contribution were not as good as the fits with the longer Fe distance except for **EXAFS4** (Table 2.5, fit 4M and 4N) which had a slightly lower F value for the short Fe minimum (0.87 for 3.03 Å Fe vs. 0.94 for 3.41 Å Fe). A comparison of the final fits to the filtered data with the non-filtered data is given in Figures 2.6d and 2.7.

The ability of the second shell Fe-C parameters to mimic the second shell contribution were tested in fits to the wide backtransforms of the data. Fits consisting of N, O and a 3.0 Å C contribution had lower fit functions than the N, O and Fe fits to the data (Table 2.5, O fits), although fits with a 3.4 Å C contribution were worse (Table 2.5, P fits). Addition of C to the N/O/Fe fits to the data resulted in the same correlation effects between the Fe and C coordination numbers and distances noted before in the fits to the second shell data. The addition of C to the N, O and Fe contributions moderately improved the quality of the fit (Figure 2.6c), illustrating that something in addition to iron is required to adequately explain the data. All of the fits reported in Table 2.5 for the wide filter fit were repeated for the second first shell minimum found, corresponding to $R_N < R_O$. The same trends were seen with slightly higher F values.

2.3.2.4. Model Dependence of EXAFS Results. Given that the Fe-Fe distance obtained in the fits of the oxidized and semimet protein data was similar to that of the **FEHBPZOH** model used to extract Fe-Fe backscattering parameters, we investigated the possibility of model dependence of the fit results. These same parameters were therefore used to fit the data of the **FEHBPZO** model compound, and parameters obtained from this model were used to fit the **FEHBPZOH** data. In both cases, two Fe-Fe distances were found, the correct one and one at about 0.4 Å away, at 3.43 and 3.06 Å for **FEHBPZOH** and at 3.15 and 3.52 Å for **FEHBPZO** (see Chapter 4, Table 4.4). The

Table 2.5. Results of Wide Shell Fits[a] to the Hydroxylase Data.[b]

Sample	Window Width (Å)	Fit	N		O		Fe		C		F
			CN[c]	R(Å)	CN	R(Å)	CN	R(Å)	CN	R(Å)	
EXAFS5	0.75 - 3.20	5L	2.3	2.14	3.4	1.97					0.99
M. capsulatus - ox		5M	2.3	2.14	3.4	1.97	1.1	3.42			0.52
		5N	2.4	2.13	3.4	1.97	0.7	3.03			0.71
		5O	2.0	2.16	3.6	1.98			5.3	3.05	0.49
		5P	2.4	2.14	3.3	1.97			3.8	3.40	0.85
		5Q	2.3	2.15	3.5	1.97	1.4	3.44	3.8	3.31	0.47
		5R	2.1	2.15	3.5	1.97	0.5	3.39	3.5	3.07	0.43
		5S	1.8	2.15	3.4	1.98	0.4	2.96	5.4	3.06	0.41
EXAFS1	0.70 - 3.40	1L	2.6	2.23	3.7	2.00					0.99
M. capsulatus - sm		1M	2.6	2.23	3.7	2.00	1.0	3.43			0.62
		1N	2.3	2.22	3.6	2.00	0.7	3.04			0.72
		1O	2.9	2.23	3.8	2.00			4.8	3.06	0.63
		1P	2.5	2.23	3.7	2.00			3.9	3.40	0.85
		1Q	2.7	2.23	3.8	2.00	1.4	3.47	5.3	3.33	0.54
		1R	2.6	2.23	3.7	2.00	0.7	3.39	3.5	3.09	0.55
		1S	2.3	2.24	3.6	2.00	0.5	2.97	5.1	3.09	0.50

Table 2.5. continued

Sample	Window Width (Å)	Fit	N		O		Fe		C		F
			CN[c]	R(Å)	CN	R(Å)	CN	R(Å)	CN	R(Å)	
EXAFS2	0.70 - 3.40	2L	2.6	2.19	3.0	1.99					1.10
M. capsulatus - sm		2M	2.6	2.19	3.0	1.99	1.1	3.41			0.67
		2N	2.5	2.18	2.9	1.98	0.9	3.04			0.74
		2O	2.7	2.20	3.2	1.99			6.2	3.05	0.40
		2P	2.5	2.19	3.0	1.99			4.7	3.38	0.90
		2Q	2.7	2.20	3.2	1.99	1.8	3.47	8.6	3.32	0.47
		2R	2.7	2.20	3.2	1.99	0.3	3.34	6.2	3.06	0.37
		2S	2.7	2.20	3.2	1.99	0.1	2.99	6.0	3.05	0.40
EXAFS4[d]	0.70 - 3.30	4L	3.0	2.15	2.6	1.95					1.40
M. trichosporium - sm		4M	3.0	2.15	2.6	1.95	1.3	3.41			0.94
		4N	3.0	2.14	2.6	1.95	1.1	3.03			0.87
		4O	2.9	2.17	2.8	1.95			7.7	3.03	0.63
		4P	3.0	2.15	2.6	1.95			4.7	3.38	1.40
		4Q	3.0	2.16	2.8	1.96	2.6	3.46	11.2	3.31	0.67
		4R	3.0	2.16	2.8	1.96	0.4	3.05	6.0	3.03	0.59

[a]Fitting range $k = 4 - 12$ Å^{-1}. Errors are estimated to be about ± 0.03 Å for distances and 25% for coordination numbers.[22,23] [b]ox = oxidized; sm = semimet. [c]CN = coordination number. [d]Negative coordination numbers were obtained in fits with a long Fe-Fe and a short Fe-C distance, and with a short Fe-Fe and a long Fe-C distance.

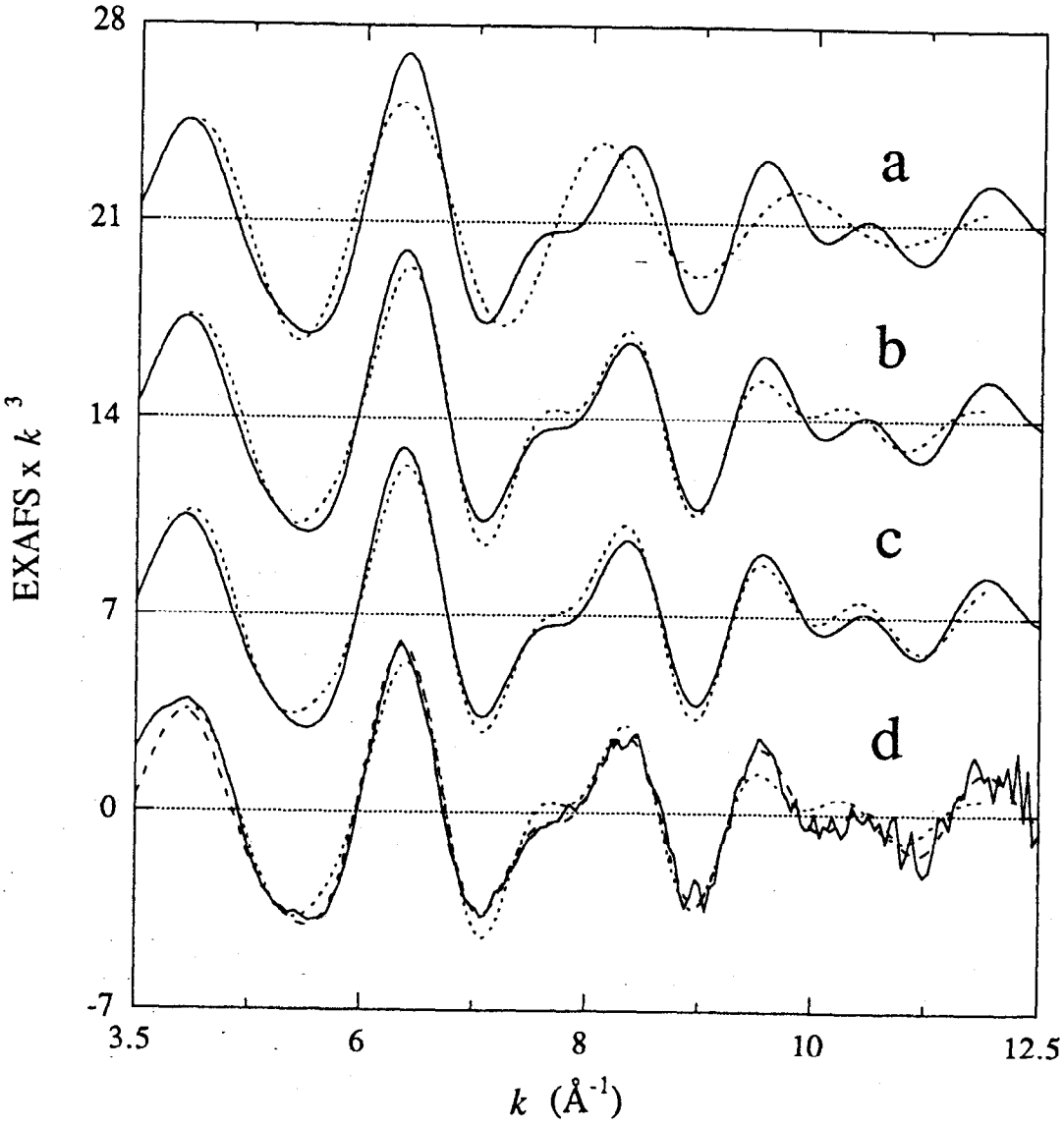

Figure 2.6. Fits to the Fourier filtered data (0.75 - 3.2 Å) for **EXAFS5**. The solid line represents the data and the dotted line is the fit. (a) Fit to the data with N and O (Table 2.5, fit 5L), (b) fit to the data with N, O and Fe (Table 2.5, fit 5M), (c) fit to the data with N, O, Fe and C (Table 2.5, fit 5R), (d) the unfiltered data (solid), the filtered data (dash) and the fit to the filtered data (dot) (Table 2.5, fit 5M).

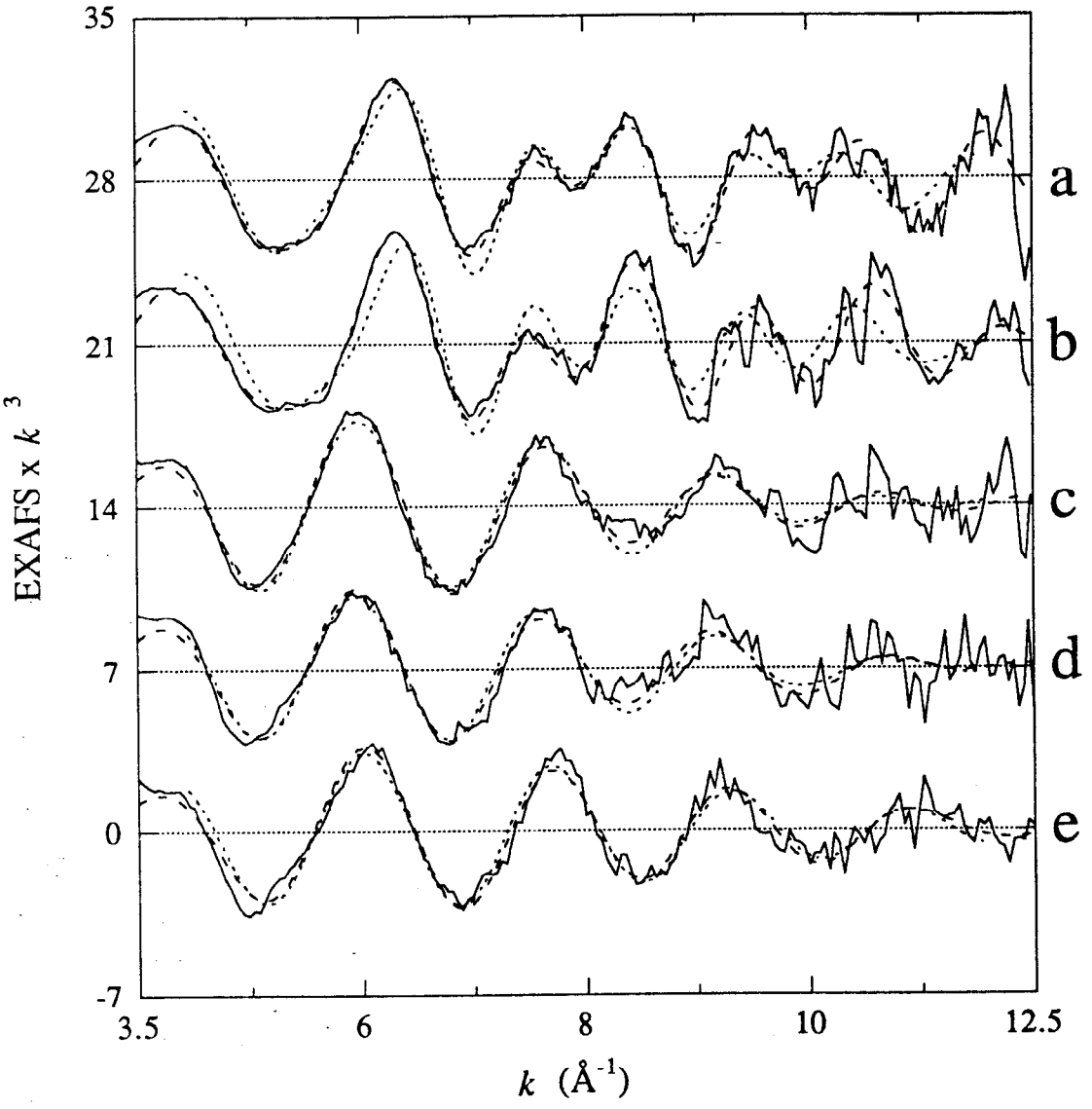

Figure 2.7. A comparison of the unfiltered data (solid), the filtered data (dash), and the fit to the filtered data (dot). (a) **EXAFS2** (Table 2.5, fit 2M), (b) **EXAFS4** (Table 2.5, fit 4M), (c) **EXAFS3** (Table 2.2, fit 3C), (d) **EXAFS6** (Table 2.2, fit 6C), (e) **RRB2** (Table 2.2, fit RR-C).

goodness-of-fit parameter, however, was lower for the longer distance obtained for the **FEHBPZO** model using Fe-Fe parameters from the hydroxo-bridged model (which has a longer Fe-Fe distance) and for the shorter distance obtained for **FEHBPZOH** using Fe-Fe parameters from the oxo-bridged model (which has a shorter Fe-Fe distance). *There is thus an apparent model dependence in which the correct distance is obtained but the results are biased to give preference to the wrong distance if a model much different from the unknown is employed.* Since first shell fits showed the absence of an oxo bridge, and the Fe-Fe and Fe-low Z scattering distances are better separated in **FEHBPZOH** vs **FEHBPZO**, we believe that the use of parameters from the hydroxo-bridged model, **FEHBPZOH**, is most appropriate and that the 3.42 Å distance is correct. While the absence of an oxo-bridge is clear, it remains to be established whether our current approach would successfully distinguish highly correlated Fe-Fe and Fe-C backscattering contributions at the same distance for well characterized complexes containing the $Fe_2(OR)_2$ bridge unit.[27] The apparent model dependence of the second shell fits to dinuclear non-heme iron data, an effect which has also been addressed by others,[28] warrants careful consideration of the model used in the determination of Fe-Fe distances in dinuclear iron centers. An investigation of this effect is presented in Chapter 4.

2.3.2.5. Fits to the Unfiltered Data. These fits were repeated for the unfiltered data between $k = 4$ and 12 $Å^{-1}$ (Table 2.6). Although the quality of the fits was generally worse due to the increased noise level of the unfiltered data, the results of the fits were essentially the same as those reported for the wide shell fits in Table 2.5 for **EXAFS1, EXAFS2, EXAFS4, EXAFS5,** and for the first shell fits in Table 2.2 for reduced samples **EXAFS3** and **EXAFS6**. Some variation in the coordinaiton numbers of the low Z atoms were seen, however the total coordination number changed very little. The fits for the raw data, the wide shell data and the filtered data are thus consistent.

2.3.2.6. Fits over a Shorter Data Range. Beyond $k = 10$ $Å^{-1}$ the EXAFS data became increasingly noisy and beyond $k = 13$ $Å^{-1}$ the data was unusable. To verify that the results obtained for the $k = 4$ - 12 $Å^{-1}$ fits were not influenced by the increasing noise of the data between 10 and 12 $Å^{-1}$, the data from 3.5 - 10.5 $Å^{-1}$ was Fourier transformed into R space and fit between 3.8 and 10 $Å^{-1}$. In general, the sum of low-Z coordination in the first shell decreased and was closer to 5 than 6, and the Fe coordination decreased to about 1 for the 3.4 Å distance. Most importantly, fits to the shorter k range for the oxidized and semimet protein samples with N, O and Fe showed a strong preference for the long Fe-Fe distance. The fit with N, O and C was no longer better than the long Fe-Fe fit. In addition, the correlation of the second shell C and Fe parameters was not as strong over the shorter data range. The Fe-Fe distances stayed closer to the values found

Table 2.6. Results of Fits[a] to the Non-Filtered Hydroxylase EXAFS.[b]

Sample	Fit	N		O		Fe		C		F
		CN[c]	R(Å)	CN	R(Å)	CN	R(Å)	CN	R(Å)	
EXAFS5	5T	2.4	2.14	3.4	1.97					1.04
M. capsulatus - ox	5U	2.3	2.14	3.4	1.97	1.1	3.42			0.62
	5V	2.0	2.15	3.4	1.97	0.6	3.37	4.2	3.08	0.52
EXAFS1	1T	2.3	2.23	3.7	2.00					1.2
M. capsulatus - sm	1U	2.3	2.23	3.7	2.00	1.0	3.43			0.89
	1V	2.1	2.21	3.5	1.99	0.9	3.42	1.4	2.64	0.85
EXAFS2	2T	2.6	2.19	3.0	1.99					1.2
M. capsulatus - sm	2U	2.6	2.19	3.0	1.99	1.1	3.41			0.74
	2V	2.7	2.20	3.2	1.99	0.3	3.35	5.9	3.06	0.53
EXAFS4[d]	4T	3.0	2.15	2.6	1.95					1.5
M. trichosporium- sm	4U	3.0	2.15	2.6	1.95	1.4	3.41			1.1
EXAFS3	3E	2.2	2.24	3.0	2.08					0.69
M. capsulatus - red										
EXAFS6	6E	2.2	2.23	2.4	2.08					0.77
M. capsulatus - red										
RRB2	RR-E	1.6	2.26	3.1	2.08					0.79
ribonucleotide reductase-red										

[a]Fitting range k = 4 - 12 Å^{-1}. Errors are estimated to be about ± 0.03 Å for distances and 25% for coordination numbers.[22,23] [b]ox = oxidized; sm = semimet; red = reduced. [c]CN = coordination number. [d]Fits to the data with a long Fe and short C contribution resulted in negative coordination numbers.

for the N, O, Fe fits to the data when C was added to the fit.

2.3.3. Results of Fits to the Ribonucleotide Reductase EXAFS Data

The EXAFS of the **RRB2** sample (Figure 2.2f) and the reduced hydroyxlase samples (Figure 2.2d,e) are very similar although the quality of the **RRB2** data is better in the higher k range, suggesting that the diiron centers in the two proteins have similar structrues There is a slight difference in the depth of the minimum above $k = 8$ Å^{-1}. The Fourier transforms of the data ($k = 3.5$ - 12.5 Å^{-1}) are also very similar (Figure 2.3d-f). Most interestingly, there is also no indication of a strong second shell contribution to the **RRB2** data.

The results of fits to the filtered first shell data are presented in Table 2.2. As noted above, more than one contribution was required to fit the first shell data and in fits with two contributions, more than one minima was found (Table 2.2, fit RR-C and RR-D), depending on the initial values of R_N and R_O. The average first shell coordination was found to be (for $R_N > R_O$) 4.3 N/O at 2.13 Å. The filtered data, the fit to the filtered data and the non-filtered data are compared in Figure 2.7e.

2.4. Discussion

2.4.1. Nature of the Hydroxylase Active Site

The first shell data required two contributions to adequately fit the data, suggesting that the first shell contains atoms at different distance distributions. This in turn means the Fe atoms are located in a somewhat distorted environment. The EXAFS analysis clearly indicates the absence of a μ-oxo bridge in the iron center of the diferric and semimet hydroxylase. The results are consistent with mixed N and O ligation to the iron atoms in the first coordination sphere. The average first shell distance for the oxidized hydroxylase was found to be 2.04 Å, and for the semimet hydroxylase samples, the average first shell distance was 2.06 - 2.09 Å. The EXAFS, Fourier transforms and fit results of the Fe(II)Fe(III) protein samples from both the *M. capsulatus* (Bath) and *M. trichosporium* OB3b samples (**EXAFS1**, **EXAFS2** and **EXAFS4**, Figure 2.1d,e and Figure 2.2b,c) are very similar, suggesting that the diiron centers in the two hydroxylases are also structurally similar. For the reduced hydroxylase samples, the average first shell distance was determined to be 2.15 Å, and the average coordination number was somewhat lower than the value for the oxidized and semimet samples.

In fits to the second shell data with either an Fe or a C contribution, two minima were found at ~ 3.0 and 3.4 Å. It is difficult to obtain unique fits to second coordination sphere EXAFS in dinuclear metalloproteins because the second shell generally contains carbon, nitrogen and/or oxygen scatterers at radial distances near that of the metal-metal separation. These low-Z contributions are difficult to model adequately because of the typical wide distribution of distances. If well-ordered, the contribution of 4-6 such low-Z scatterers can be approximately of the same magnitude as that of a single metal scatterer. Although the backscattering envelope from Fe should maximize at higher k values than envelopes from low-Z scatterers, interference among several shells of low-Z scatterers can effectively change the expected decreasing contribution to the EXAFS at higher k, and make the backscattering envelope of low-Z scatterers appear quite similar to that of the metal.[29] The use of C backscattering parameters derived from $Fe(acac)_3$ to model the low-Z contribution to second shell data has often been described in the literature; however, its backscattering envelope is similar to that of a first row transition metal, most likely because of interference of its two closely lying C second shells (Figure 2.8), resulting in the adequate fits to the second shell data with C and no Fe contribution. This phenomenon has been observed by others in fits to dinuclear non-heme iron models[30] and dinuclear copper and mixed copper-iron dimers.[29]

For bridged dinuclear model compounds, the second coordination sphere normally contains a large number of low-Z atoms spread around 3.0 Å, always at a shorter distance than, and independent of, the Fe-Fe distance.[16] It is, however, quite unlikely in any Fe coordination environment that outer C shells would be so ordered that they give an EXAFS contribution as large as those seen for the oxidized and semimet hydroxylase samples. For example, even in Fe(TPP), which has 8 well-ordered α-carbon atoms, the second shell peak in the Fourier transform is only about 1/3 the height of the first shell peak.[31] It would thus be expected that the strength of the 3.0 Å Fe-Fe distance minimum derives from accidental coincidence of the frequency decrease in the phase of the Fe wave with a distance where there is an actual strong contribution to the data from C/N/O backscatterers. The 3.4 Å distance, on the other hand, originates primarily from the Fe backscatterer, most likely mixed with other low-Z backscatterers. As has been pointed out elsewhere,[30] longer Fe-C distances are expected to contribute less distinctly to the EXAFS because they originate from three-bond Fe-C distances, and thus are expected to have high thermal disorder.

The most reasonable interpretation for the second shell results is that the second shell contains an Fe-backscatterer at a distance of about 3.42 Å for the oxidized and semimet samples, and that there is a shell of low-Z scatterers distributed around 3.05 Å.

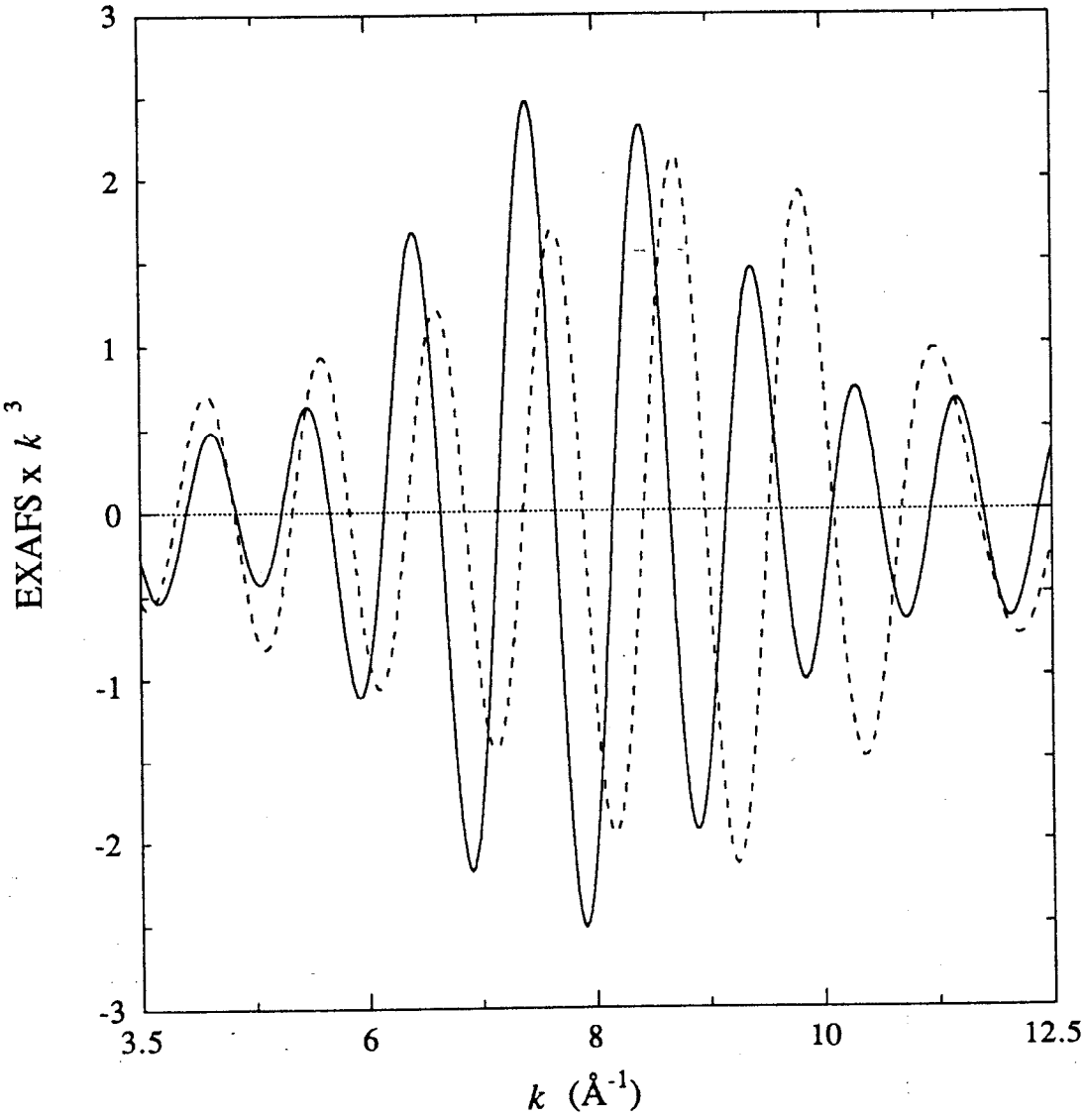

Figure 2.8. A comparison of the Fourier filtered second shell Fe-Fe data from **FEHBPZOH** (solid) and the second shell Fe-C data from $Fe(acac)_3$ (dash). Note that the Fe-C wave reaches a maximum at higher k than the Fe-Fe wave.

With Fe-N distances around 2.1-2.2 Å, the Fe-C/N second shell distances lie in the 3.0-3.2 Å range, in accord with the present observations. The presence of Fe in the second shell is compatible with EPR data showing the existence of a dinuclear iron center.[5c,15,18] The Fe-Fe distance should not be affected by intervening-atom multiple scattering effects, because the minimum Fe-O bridge distance of 2.0 Å corresponds to a maximum Fe-O-Fe angle of 129°.[32] The 3.4 Å distance is compatible with the presence of a monodentate bridging group such as hydroxide, carboxylate or alkoxide.[33] In addition, the value implies the existence of at least one other bridging group, most likely a *syn, syn* bidentate carboxylate.[33b] The J value of -32 cm^{-1} measured for the Fe(II)Fe(III) form of the hydroxylase indicates weak antiferromagnetic exchange and is consistent with hydroxo, alkoxo, or monodentate carboxylato bridging ligands.

The peak associated with the metal-metal interaction is missing for both reduced hydroxylase samples and the reduced sample of ribonucleotide reductase B2 suggesting that the cause of the reduction in the Fe-Fe backscattering peak is inherent in the structures of the samples, and not in the data collection or analysis. The absence of a resolvable iron-iron interaction in diferrous systems is not unusual. In deoxyhemerythrin, the iron-iron peak disappears upon warming the protein from 80 K to room temperature.[34] Also, no Cu(I)-Cu(I) peak is seen in the Fourier transform of deoxyhemocyanin data.[35] In addition, the Fe-Fe peak could not be resolved in the semimet form (pink) of beef spleen purple acid phosphatase.[36] This phenomenon could be caused by the loss of a bridge in the metal center upon reduction causing uncorrelated vibrations of the metal atoms (increased Debye-Waller factor), or by destructive interference in the second shell EXAFS between the Fe-Fe wave and second shell Fe-N, Fe-C and/or Fe-O waves.

The change in the Fe and C coordination numbers and distances that occur when adding a C contribution to the Fe contribution in second shell fits is a result of the correlation between the Fe-Fe and Fe-C parameters. For model compounds, the correct Fe-Fe distance is obtained when fitting with Fe alone, and a similar correlation effect is seen for fits with the same Fe-Fe and Fe-C parameters used in the protein fits (see Chapter 4). The strength in the second shell low-Z atom backscattering could arise from second shell atoms arranged in a rigid structure such as the imidazole ring (present in histidine). The presence of rigid ligands has been associated with characteristic features in the outer shell region of Fourier transforms arising from contributions to the data from multiple scattering pathways. The means by which to model the multiple scattering contributions are still being developed.[37] The relatively weak outer shell features in the hydroxylase samples suggest that such groups are not contributing significantly, therefore these approaches have not yet been attempted.

In addition to determining the nature of the bridge and the Fe-Fe separation in the active site of the MMO hydroxylase, the coordination of the iron atoms in the active site is of interest. The value of the quadropole splitting (ΔE_Q) obtained by Mössbauer studies, was 1.05 mm/s which is larger than the quadropole splittings for hydroxo-bridged model compounds and smaller than oxo-bridged iron centers.[18] The intermediate value can be interpreted as meaning that the Fe-O_{bridge} distance is intermediate between an oxo-bridge distance and a hydroxo-bridge distance, or that the iron atoms are penacoordinate and/or in a highly distorted octahedral environment. Although fits to the first shell EXAFS of the diferric protein suggest that the coordination number of the iron atoms is approximately six, it should be noted that EXAFS results represent the average of two not necessarily identical iron centers, and therefore may not readily distinguish between five- and six-coordinate iron atoms.

2.4.2. Comparison to Proteins Containing Diiron Cores

The spectroscopic similarities of the non-heme dinuclear iron proteins (Hr, RRB2, PAP, Uf, and MMO) suggest that the active site structures may also be similar. A comparison of EXAFS studies of RRB2[30,38] with those on crystallographically characterized Hr[30,34,39], have suggested that the two proteins possess similar active sites, consisting of a pair of triply-bridged iron atoms at a separation on the order of 3.2 Å in the diferric form, with a μ-oxo bridge and two *syn,syn* bidentate carboxylate bridges. Recently, crystallographic characterization of RRB2 revealed the presence of one, not two, bridging carboxylates.[40] The average first shell coordination of oxyHr consists of 5 N and O atoms at 2.15 - 2.16 Å while the average first shell coordination of diferric RRB2 consists of 5 N and O atoms at 2.04 - 2.06 Å (excluding the oxo-bridge distance). In general, Fe-N bond lengths are longer than Fe-O bond lengths in iron complexes; the shorter average distance in the first shell coordination of RRB2 compared to oxyHr suggests that there are fewer nitrogens and more oxygens coordinated to the iron atoms in RRB2 than in oxyHr.[38] The crystal structure has confimed that there are just two histidines ligands coordinated to the iron atoms in RRB2,[40] as compared to five histidines in Hr.[41] The average distance in the first coordination shell of the diferric form of MMO was found to be 2.01 - 2.04 Å, suggesting that like RRB2, there are more oxygens and fewer nitrogens coordinated to the iron atoms in MMO than in oxyHr. Unlike both diferric centers in RRB2 and oxyHr, there is no μ-oxo bridge in the dinuclear iron center of MMO and the Fe-Fe distance, determined to be 3.42 Å, is longer than the Fe-Fe distance in either

of those proteins, as one would expect for a di- or tri-bridged complex without an oxo bridge.

No evidence for a μ-oxo bridge was found in the diferric form of beef spleen PAP (purple), although the presence of short Fe-O (tyrosine) bonds in the protein could have obscured the contribution of the Fe-O (bridge) chromophore to the data,[36] and therefore the possibility of an oxo bridge could not be ruled out. An Fe-Fe distance of 3.00 Å was deduced by the FABM curve fitting technique with parameters obtained by using a mono-bridged (μ-oxo)diiron(III) model compound. The first shell coordination was similar to that reported here for MMO (Table 2.2, fit 5C), with 3.0 N/O at 2.13 Å and 3.5 N/O at 1.98 Å, or an average of 6.5 N/O at 2.05 Å. EXAFS analysis of the diferric center in phosphate and arsenate bound forms of porcine uterine puple acid phosphatase (uteroferrin, Uf) have established that the diiron center does not contain a μ-oxo bridge.[42] The average first shell coordination was found to be 6 N/O at 2.10 - 2.14 Å, suggesting either that there is greater N ligation to the iron center in Uf relative to MMO, or that the ligation of the phosphate and arsenate anions distorts the iron center. The Fe-Fe distance was found to be 3.2 - 3.3 Å.

EXAFS analysis of the oxidized hydroxylase from *Methylobacterium* CRL-26 indicated an Fe-Fe distance of 3.05 Å by using model corrected theoretical amplitude and phase parameters, while no evidence for or against an oxo bridge in the first shell was found owing to the limited range of the data.[17] This value disagrees with the Fe-Fe distance found in the present study for the same protein from a different species. Although it is possible that this difference is real, implying structurally different dinuclear iron centers, the discrepancy may arise from differences in analysis protocol. The first shell coordination of the hydroxylase from *Methylobacterium* CRL-26 consisted of 4 - 6 N/O at an average distance of 1.92 Å. This distance is much shorter than that found for any other diferric protein.

The average increase of 0.04 Å in the first shell coordination distance upon photoreduction to the semimet state of MMO is similar to the increase in the average coordination sphere for oxidized PAP (purple) upon conversion to its one electron reduced (pink) form (6.0 N/O at 2.08 Å).[36] The Fe-Fe distance of 3.41 - 3.43 Å is slightly shorter than the Fe-Fe distance found for semimethemerythrin azide.[30] Although one would expect the Fe-Fe distance to lengthen upon reduction of the diferric hydroxylase to the semimet form, our fit results do not show this trend. This suggests that the structure of the iron core does not change as much as the hemerythrin core in met- and semimethemerythrin azide[30] with reduction. It is also possible that improvement of the carbon backscattering parameters could give more precise results.

Plots of individual contributions to the wide shell fits showed that the differences in the EXAFS at ~ 7 and 11 Å for the oxidized and semimet samples are caused by changes in the N/O wave interaction with a more or less constant Fe wave. For the oxidized sample, the Fe wave at ~ 7 and 11 Å maximizes almost directly on top of minima in the N/O wave, giving rise to the weak shoulder in the data at those two points relative to data for the semimet hydroxylase. For the semimet sample, the N/O wave has shifted to lower frequency and the Fe wave maxima at the two points in question are no longer at a location corresponding to N/O minima, resulting in peak-like features. Due to the limited range of data available, the origin of the differences in the first shell data cannot be determined by EXAFS.

The average first shell coordination distance increased by an average of 0.12 Å from the diferric to the diferrous state. The data and fits for the two diferrous protein samples are essentially identical, although **EXAFS3** had higher coordination numbers than **EXAFS6**. For deoxyhemerythrin, the average first shell coordination was 2.15 Å by EXAFS analysis, similar to the average first shell coordination of the diferrous hydroxylase. The data for reduced RRB2 was very similar to the reduced hydroxylase, with a 2.13 Å average first shell distance. The peak associated with the metal-metal interaction is missing for both reduced hydroxylase protein samples and the reduced ribonucleotide reductase sample, suggesting that the absence of a Fe-Fe backscattering peak is inherent in the structure of the samples, and that therefore the active sites of the reduced hydroxylase of MMO and B2 subunit of RR may be similar. A 3.57 Å Fe-Fe distance has been reported for deoxyhemerythrin.[28]

2.5. Conclusions

MMO is similar spectroscopically to the other non-heme dinuclear iron proteins, however the EXAFS results clearly show that the active site structure is different from that in Hr and RRB2. Specifically, the hydroxylase of MMO does not have a μ-oxo bridge in its iron center. The 3.4 Å Fe-Fe separation and the absence of the short Fe-O bridge suggest that the iron atoms may contain an alkoxo, hydroxo or monodentate carboxylato bridge and one or two bidentate carboxylato bridges. The coordination number of the iron atoms is suggested to be 6, however this determination is not conclusive. In addition, the average first shell distance of 2.04 Å suggests that there are fewer histidine ligands in the iron center of MMO than in Hr.

The determination of the second coordination sphere of the hydroxylase data has proven to be a non-trivial problem. The **FEHBPZOH** model is more likely to represent

the protein active site than the **FEHBPZO** model, however, the apparent model-dependence of second shell fits to the data warrants caution regarding conclusions about Fe-Fe distances in dinuclear centers. Based on the information available, the most reasonable interpretation of the second shell data is that the Fe-Fe distance is ~ 3.4 Å and that there is a shell of low Z atoms at ~ 3.0 Å from the iron center.

2.6. Acknowledgements

The data were collected at the Stanford Synchrotron Radiation Laboratory and the National Synchrotron Light Source, Brookhaven National Laboratory, which are supported by the Department of Energy, Office of Basic Energy Sciences, Division of Chemical Sciences and Division of Materials Sciences. SSRL is also supported by the National Institutes of Health, Biomedical Resource Technology Program, Division of Research Resources. Grant support was provided by the National Science Foundation (CHE 88-17702 to KOH), the Gas Research Institute (5086-260-1209 to HD), and the National Institute of General Medical Sciences (GM 32134 to SJL).

2.7. References and Notes

1. Anthony, C. *The Biochemistry of the Methylotrophs*; Academic Press: London, 1982.

2. (a) Higgins, I. J.; Best, R. C.; Scott, D. *Microbiol. Reviews* **1981**, *45*, 556-590. (b) Whittenbury, R.; Phillips, K. C.; Wilkinson, J. F. *J. Gen. Microbiol.* **1970**, *61*, 205-218.

3. (a) Prior, S. D.; Dalton, H. *J. Gen. Microbiol.* **1985**, *131*, 155-163. (b) Dalton, H.; Prior, S. D.; Leak, D. J. *Microb. Growth on C1 Cmpd., Proc. Int. Symp., 1983*; Am. Soc. Microbiol.: Washington D. C., 1984; pp. 75-82. (c) Stanley, S. H.; Prior, S. D.; Leak, D. J.; Dalton, H. *Biotech. Lett.* **1983**, *5*, 487-492.

4. Tonge, G. M.; Harrison, D. E. F.; Higgins, I. J. *Biochem J.* **1977**, *161*, 333-344.

5. (a) Colby, J.; Dalton, H. *Biochem. J.* **1976**, *157*, 495-497. (b) Stirling, D. I.; Dalton, H. *J. Biochem.* **1979**, *96*, 205-212. (d) Patel, R. N. *Microb. Growth on C1 Cmpd., Proc. Int. Symp. 1983*; Am. Soc. Microbiol.: Washington D. C., 1984; pp. 83-90.

6. (a) Colby, J.; Stirling, D. I.; Dalton, H. *Biochem. J.* **1977**, *165*, 395-402. (b) Hou, C. T.; Patel, R. N.; Laskin, A. I.; Barnabe, N. *FEMS Microbiol. Lett.* **1980**, *9*, 267-270. (c) Leak, D. J.; Dalton, H. *J. Gen. Microbiol.* **1983**, *129*, 3487-3497. (d) Fox, B. G.; Borneman, J. G.; Wackett, L. P.; Lipscomb, J. D. *Biochemistry* **1990**, *29*, 6419-6427. (e) Stirling, D. I.; Colby, J.; Dalton, H. *Biochem. J.* **1979**, *177*, 361-364.

7. Colby, J.; Dalton, H. *Biochem. J.* **1978**, *171*, 461-468.

8. (a) Patel, R. N.; Savas, J. C. *J. Bacteriol.* **1987**, *169*, 2313-2317. (b) Patel, R. N. *Arch. Biochim. Biophys.* **1987**, *252*, 229-236.

9. (a) Colby, J.; Dalton, H. *Biochem. J.* **1979**, *177*, 903-908. (c) Lund, J.; Dalton, H. *Eur. J. Biochem.* **1985**, *147*, 292-296. (d) Prince, R. C.; Patel, R. N. *FEBS* **1986**, *203*, 127-130.

10. (a) Woodland, M. P.; Dalton, H. *Anal. Biochem.* **1984**, *139*, 459-462. (b) Woodland, M. P.; Dalton, H. *J. Biol. Chem.* **1984**, *259*, 53-59. (c) Fox, B. G.; Lipscomb, J. D. *Biochem. Biophys. Res. Comm.* **1988**, *154*, 165-170.

11. (a) Lund, J.; Woodland, M. P.; Dalton, H. *Eur. J. Biochem.* **1985**, *147*, 297-305. (b) Green, J.; Dalton, H. *Biochem. J.* **1986**, *236*, 155-162. (c) Green, J.; Dalton, H. *Biochem. J.* **1989**, *259*, 167-172.

12. Green, J.; Dalton, H. *J. Biol. Chem.* **1985**, *260*, 15795-15801.

13. Woodland, M. P.; Patil, D. S.; Cammack, R.; Dalton, H. *Biochim. Biophys. Acta* **1986**, *873*, 237-242.

14. (a) Lippard, S. J. *Angew. Chem. Int. Ed. Engl.* **1988**, *27*, 344-361. (b) Sanders-Loehr, J. *Iron Carriers and Iron Proteins*; VCH Publishers Inc.: New York, 1989; pp. 373-466.

15. (a) Ericson, A.; Hedman, B.; Hodgson, K. O.; Green, J.; Dalton, H.; Bentsen, J. G.; Beer, R. H.; Lippard, S. J. *J. Am. Chem. Soc.* **1988**, *110*, 2330-2332. (b) DeWitt, J.; Hedman, B.; Ericson, A.; Hodgson, K. O.; Bentsen, J.; Beer, R.; Lippard, S. J.; Green, J.; Dalton, H. *Physica B* **1989**, *158*, 97-98.

16. Hedman, B.; Co, M. S.; Armstrong, W. H.; Hodgson, K. O.; Lippard, S. J. *Inorg. Chem.* **1986**, *25*, 3708-3711.

17. Prince, R. C.; George, G. N.; Savas, J. C.; Cramer, S. P.; Patel, R. N. *Biochim. Biophys. Acta* **1988**, *952*, 220-229.

18. DeWitt, J. G.; Bentsen, J. G.; Rosenzweig, A. C.; Hedman, B.; Green, J.; Pilkington, S.; Papaefthymiou, G. C.; Dalton, H.; Hodgson, K. O.; Lippard, S. J. *J. Am. Chem. Soc.* **1991**, *113*, 9219-9235.

19. This is the same data set as reported in ref. 15a; the data have been reanalyzed over the same range and with the same empirical amplitude and phase parameters used for the other samples in this paper for direct comparison.

20. (a) Stern, E. A.; Heald, S. M. *Rev. Sci. Instr.* **1979**, *50*, 1579-1582. (b) Lytle, F. W.; Greegor, R. B.; Sandstrom, D. R.; Marques, E. C.; Wong, J.; Spiro, C. L.; Huffman, G. P.; Huggins, F. E. *Nucl. Instr. Meth.* **1984**, *226*, 542-548.

21. Cramer, S. P.; Tench, O.; Yocum, M.; George, G. N. *Nucl. Instr. Meth. Phys. Res.* **1988**, *A266*, 586-591.

22. (a) Scott, R. A. *Meth. Enzymol.* **1985**, *117*, 414-459. (b) Cramer, S. P.; Hodgson, K. O.; Stiefel, E. I.; Newton, W. E. *J. Am. Chem. Soc.* **1978**, *100*, 2748-2761. (c) Cramer, S. P.; Hodgson, K. O. *Prog. Inorg. Chem.* **1979**, *15*, 1-39.

23. Scott, R. A.; Hahn, J. E.; Doniach, S.; Freeman, H. C.; Hodgson, K. O. *J. Am. Chem. Soc.* **1982**, *104*, 5364-5369.

24. (a) Iball, J.; Morgan, C. H. *Acta Cryst.* **1976**, *23*, 239-244. (b) Roof, Jr., R. B. *Acta Cryst.* **1956**, *9*, 781-786.

25. Johansson, L. *Chem. Scr.* **1976**, *9*, 30-35. The crystal structure of the perchlorate salt has not been determined, but the $[Fe(phenanthroline)_3]^{2-}$ complex structure can be

assumed to be identical with that of the corresponding iodide salt (Johansson, L.; Molund, M.; Oskarsson, Å. *Inorg. Chim. Acta* **1978**, *31*, 117-123).

26. (a) Armstrong, W. H.; Lippard, S. J. *J. Am. Chem. Soc.* **1984**, *106*, 4632-4633. (b) Armstrong, W. H.; Spool, A.; Papaefthymiou, G. C.; Frankel, R. B.; Lippard, S. J. *J. Am. Chem. Soc.* **1984**, *106*, 3653-3667.

27. Snyder, B. S.; Patterson, G. S.; Abrahamson, A. J.; Holm, R. H. *J. Am. Chem. Soc.* **1989**, *11*, 5214-5223 and references therein.

28. Zhang, K.; Stern, E. A.; Ellis, F.; Sanders-Loehr, J.; Shiemke, A. K. *Biochemistry* **1988**, *27*, 7470-7479.

29. Scott, R. A.; Eidsness, M. K. *Comments Inorg. Chem.* **1988**, *7*, 235-267.

30. Scarrow, R. C.; Maroney, M. J.; Palmer, S. M.; Que, L. Jr.; Roe, A. L.; Salowe, S. P.; Stubbe, J. *J. Am. Chem. Soc.* **1987**, *109*, 7857-7864.

31. Cramer, S. P. Ph.D. Thesis, Stanford University, 1977.

32. Co, M. S.; Hendrickson, W. A.; Hodgson, K. O.; Doniach, S. *J. Am. Chem. Soc.* **1983**, *105*, 1114-1150.

33. (a) Kurtz, D. M., Jr. *Chem. Rev.* **1990**, *90*, 585-606. (b) Rardin, R. L., Jr.; Tolman, W. B.; Lippard, S. J. *New J. Chem.* **1991**, *15*, 417-430.

34. Elam, W. T.; Stern, E.A.; McCallum, J. D.; Sanders-Loehr, J. *J. Am. Chem. Soc.* **1983**, *105*, 1919-1923.

35. Co, M. S.; Hodgson, K. O. *J. Am. Chem. Soc.* **1981**, *103*, 3200-3201.

36. Kauzlarich, S. M.; Teo, B. K.; Zirino, T.; Burman, S.; Davis, J. C.; Averill, B. A. *Inorg. Chem.* **1986**, *25*, 2781-2785.

37. (a) Co, M. S.; Scott, R. A.; Hodgson, K. O. *J. Am. Chem. Soc.* **1981**, *103*, 986-988. (b) Hasnain, S. S.; Ed. *Synchrotron Radiation and Biophysics*; Ellis Horwood Ltd.: Chichester, 1990; Chapters 3 and 4.

38. (a) Scarrow, R. C.; Maroney, M. J.; Palmer, S. M.; Que, L. Jr.; Salowe, S. P.; Stubbe, J. *J. Am. Chem. Soc.* **1986**, *108*, 6832-6834. (b) Bunker, G.; Petersson, L.; Sjöberg, B.-M., Sahlin, M.; Chance, M.; Chance, B.; Ehrenberg, A. *Biochemistry* **1987**, *26*, 4708-4716.

39. (a) Hendrickson, W. A.; Co, M. S.; Smith, J. L.; Hodgson, K. O.; Klippenstein, G. L. *Proc. Natl. Acad. Sci. USA* **1982**, *79*, 6255-6259. (b) Elam, W. T.; Stern, E. A.; McCallum, J. D.; Sanders-Loehr, J. *J. Am. Chem. Soc.* **1982**, *104*, 6369-6373. (c) Maroney, M. J.; Scarrow, R. C.; Que, L. Jr.; Roe, A. L.; Lukat, G. S.; Kurtz, D. M. Jr. *Inorg. Chem.* **1989**, *28*, 1342-1348.

40. (a) Nordlund, P.; Uhlin, U.; Westergren, C.; Joelsen, T.; Sjöberg, B.-M.; Eklund, H. *FEB* **1989**, *258*, 251-254. (b) Nordlund, P.; Sjöberg, B.-M.; Eklund, H. *Nature*, **1990**, *345*, 593-598.

41. (a) Stenkamp, R. E.; Sieker, L. C.; Jensen, L. H.; McCallum, J. D.; Sanders-Loehr, J. *Proc. Natl. Acad. Sci. USA* **1985**, *82*, 713-716. (b) Stenkamp, R. E.; Sieker, L. C.; Jensen, L. H. *J. Am. Chem. Soc.* **1984**, *106*, 618-622.

42. True, A. E., Scarrow, R. C.; Holz, R. C.; Que, L., Jr. *Inorg. Biochem.* **1991**, *43*, 545, and personal communication.